รายงานวิจัยฉบับสมบูรณ์

โครงการ การสร้าง สมบัติทางแม่เหล็ก ทางไฟฟ้าและเชิงกลของอนุภาคผงนาโนแม่เหล็ก $CoFe_2O_4$ และการใช้เสริมแรงวัสดุจีโอพอลิเมอร์

โดย ผู้ช่วยศาสตราจารย์ ดร.สิทธิ์ชัย หันประทับ

กันยายน 2562

สัญญาเลขที่ TRG598003

รายงานวิจัยฉบับสมบูรณ์

โครงการ การสร้าง สมบัติทางแม่เหล็ก ทางไฟฟ้าและเชิงกลของอนุภาคผงนาโนแม่เหล็ก $CoFe_2O_4$ และการใช้เสริมแรงวัสดุจีโอพอลิเมอร์

ผู้ช่วยศาสตราจารย์ ดร.สิทธิ์ชัย หันประทับ

มหาวิทยาลัยราชภัฏอุดรธานี

สนับสนุนโดยสถาบันวิจัยแสงซินโครตรอน (องค์การมหาชน)

และ สำนักงานกองทุนสนับสนุนการวิจัย (สกว.)

(ความเห็นในรายงานนี้เป็นของผู้วิจัย สถาบันวิจัยแสงซินโครตรอน (องค์การมหาชน) และ สกว. ไม่จำเป็นต้องเห็นด้วยเสมอไป)

บทคัดย่อ

รหัสโครงการ: TRG598003

ชื่อโครงการ: การสร้าง สมบัติทางแม่เหล็ก ทางไฟฟ้าและเชิงกลของอนุภาคผงนาโนแม่เหล็ก $CoFe_2O_4$ และการใช้เสริมแรงวัสดุจีโอพอลิเมอร์

ชื่อนักวิจัย: ผู้ศาสตราจารย์ ดร.สิทธิ์ชัย หันประทับ มหาวิทยาลัยราชภัฏอุดรธานี

E-mail Address: sitchaihunpratub@gmail.com

ระยะเวลาโครงการ: 2 ปี

งานวิจัยนี้ศึกษาคุณสมบัติการผลิตสมบัติทางไฟฟ้า แม่เหล็กและเชิงกล ของวัสดุผสมนาโนแม่เหล็ก $CoFe_2O_4$ และจีโอโพลีเมอร์ เพื่อประยุกต์ใช้ในงานวิศวกรรมโยธา วัสดุผงนาโนแม่เหล็ก $CoFe_2O_4$ เตรียมโดยวิธีการตกตะกอนร่วมที่ค่า pH 9, 11 และ 14 ตัวอย่างผงแคลไซน์ที่อุณหภูมิ 300, 500 และ 700 $^{\circ}C$ เป็นเวลา 1 ชั่วโมงในอากาศ ผลจากการศึกษาด้วย XRD พบว่า ทุกตัวอย่างมีเฟสที่บริสุทธิ์ยกเว้นตัวอย่างที่เตรียมที่ pH 9 และเผาแคลไซน์ที่อุณหภูมิ 500 และ 700 $^{\circ}C$ ซึ่งมีการปนเปื้อนของ Fe_2O_3 ผลจากการศึกษาด้วย XANES พบว่า สถานะเวเลนซ์ของไอออน Co และ Fe ใกล้เคียงกับธาตุมาตรฐาน CoO (Co^{2+}) และ Fe_2O_3 (Fe^{3+}) ซึ่งสอดคล้องกับผลจากการศึกษาด้วย XPS พบว่า สเปคตรัมของ Co 2p แสดงสองยอดพีคที่ ~ 796 eV และ ~ 780 eV แสดงให้เห็นว่า Co อยู่ในสถานะ 2+ และสเปคตรัมของ Fe 2p แสดงสองยอดพีคที่ ~ 711 eV และ ~ 724 eV แสดงว่า Fe อยู่ในสถานะ 3+ ผลจากการศึกษาด้วย TEM พบว่า ขนาดอนุภาคเฉลี่ยของตัวอย่างอยู่ในช่วงตั้งแต่ ~ 10 ถึง ~ 38 นาโนเมตร ผลจากการศึกษาด้วย VSM พบว่า วัสดุผง $CoFe_2O_4$ ทั้งหมดแสดงพฤติกรรมทางแม่เหล็กแบบเฟอร์โร ที่อุณหภูมิห้อง โดยที่ค่าอิ่มตัวทางแม่เหล็กมีค่าสูงขึ้นเมื่ออุณหภูมิในการเผาเพิ่มขึ้นและอิ่มตัวทางแม่เหล็กสูงสุดที่ 71.9 emu / g และค่าสนามแม่เหล็กคงค้างที่ 1,540 Oe สำหรับวัสดุผง $CoFe_2O_4$ ที่สังเคราะห์ที่ pH 11 และเผาที่ 700 $^{\circ}C$ ผลจากการศึกษาค่าคงที่ไดอิเล็กทริกตามความถี่ของวัสดุผสม $CoFe_2O_4$ และจีโอโพลีเมอร์ พบว่า มีค่าลดลงอย่างรวดเร็วเมื่อความถี่เพิ่มขึ้น ผลจากการศึกษาการพล็อต Nyquist วัสดุผสม $CoFe_2O_4$ และจีโอโพลีเมอร์ที่อายุ 28 วัน พบว่า ประกอบด้วยสองส่วน คือ ผลของความต้านทานในตัวอย่าง และผลของอิเล็กโทรด โดยผลของความต้านทานในตัวอย่างสามารถหาได้จากจุดตัดแกนจริงของค่าความต้านทางเชิงซ้อน และมีค่าเท่ากับ 250, 150, 165 และ 180 สำหรับการเติมอนุภาคนาโน $CoFe_2O_4$ ที่ 0, 1, 3 และ 5% โดยน้ำหนัก ตามลำดับ ผลจากการศึกษากำลังอัดรับแรงอัดของวัสดุผสม $CoFe_2O_4$ และจีโอโพลีเมอร์ พบว่า มีค่าเท่ากับ 47.3, 42.5, 42.7 และ 49.5 สำหรับการเติมอนุภาคนาโน $CoFe_2O_4$ ที่ 0, 1, 3 และ 5% โดยน้ำหนัก ตามลำดับ ซึ่งกำลังรับแรงอัดลดลงเมื่อเติมอนุภาคนาโน $CoFe_2O_4$

และเพิ่มขึ้นอีกครั้งเมื่อเพิ่มอนุภาคนาโน $CoFe_2O_4$ ถึง 5% ค่ากำลังรับแรงอัดสูงกว่าของจีโอโพลีเมอร์ที่ไม่มีอนุภาคนาโน $CoFe_2O_4$ เนื่องจากอนุภาคนาโน $CoFe_2O_4$ เขาไปเติมในช่องว่างของโครงสร้างของเจล N-A-S-H ทำให้ตัวอย่างมีความหนาแน่นสูงขึ้นและอัดตัวกันแน่นมากขึ้น

คำหลัก : จีโอพอลิเมอร์, อนุภาคผงนาโน, สมบัติแม่เหล็กแบบเฟอร์โร

ABSTRACT

Project Code: TRG598003

Project Title: Fabrication, electrical, magnetic and mechanical properties of ferromagnetic $CoFe_2O_4$ nanopowders and their use as reinforcement of geopolymer

Investigator: Assistant Professor Dr. Sitchai Hunpratub
Udon Thani Rajabhat University

E-mail Address: sitchaihunpratub@gmail.com

Project Period: 2 year

This work investigates the fabrication, electrical, magnetic and mechanical properties of ferromagnetic $CoFe_2O_4$ nanopowders and geopolymer composites for application in civil structure. The $CoFe_2O_4$ nanopowders are prepared by co-precipitation method at pH values of 9, 11 and 14. The powder samples calcined at temperatures of 300, 500 and 700 $^{\circ}$C for 1 h in air. The XRD results, all samples have purity phase, except the samples prepared at a pH of 9 and calcined at temperatures of 500 and 700 $^{\circ}$C exhibited an impurity phase which could be associated with Fe_2O_3. The XANES results, the edge positions for all samples were close to those of the CoO (Co^{2+}) and Fe_2O_3 (Fe^{3+}) standards, indicating that these were the valence states of most of the Co and Fe ions. XPS measurements were carried out to investigate the electronic state. The Co 2p and Fe 2p spectra are deconvoluted for the quantitative analyses. In high resolution Co 2p spectra, the two peaks assigned at ~796 eV and ~780 eV are demonstrating that Co is in 2+ state. The peaks situated at ~711eV and ~724 eV indicates that Fe is in 3+ state. The TEM results indicated that the average particle sizes of the samples were in the range from ~10 to ~38 nm. All the $CoFe_2O_4$ samples exhibited ferromagnetic behavior at room temperature, with M_S increasing with increasing calcination temperature for all pH concentrations and exhibited the highest M_S value at 10 kOe of 71.9 emu/g and an H_C value of 1540 Oe for synthesis at a pH of 11 and calcination at 700°C. The values of dielectric constant as functions of frequency for the $CoFe_2O_4$–geopolymer composites. The values of dielectric constant rapidly decreased with the increased frequency. The Nyquist plots of geopolymer composites at the age of 28 day. Two parts were observed which can be identified as bulk resistance, fly ash resistance and electrode resistance. The bulk resistance was

observed from intercept on real axis at high frequency and found to be 250, 150, 165 and 180 for 0, 1, 3 and 5% of $CoFe_2O_4$ nanopowders, respectively. The compressive strength, plotting as a function of $CoFe_2O_4$ nanoparticles containing with 0, 1, 3 and 5 %wt. The compressive strength values of geopolymer composites are 47.3, 42.5, 42.7 and 49.5 for 0, 1, 3 and 5 %wt. $CoFe_2O_4$ nanoparticles, respectively. It can be seen that compressive strength deceased with the replacing $CoFe_2O_4$ nanoparticles at 1 %wt. And then the increasing quantity of $CoFe_2O_4$ nanoparticles up to 5%, the compressive strength is higher than that of geopolymer without $CoFe_2O_4$ nanoparticles for 5 %wt. $CoFe_2O_4$ nanoparticles. The strength of geopolymer increased can be described as follows that the addition of $CoFe_2O_4$ nanoparticles fills the voids of N-A-S-H gel structure are denser and compact.

Keywords : Geopolymer; Nanamagnetic; Fabrication; Electrical; Composites

1. Introduction to the research problem and its significance

The most used construction materials adaptable to a wide of civil engineering and structural designs are cement and concrete. Ordinary Portland Cement (OPC) is the common and is widely used in the construction industry. However, the production of OPC requires a large amount of energy and the process emits significant amount of carbon dioxide (CO_2) gas. In producing a ton of OPC, approximately 0.9 ton of CO_2 is released. It is estimated that 7% of greenhouse gas is produced annually from this worldwide [1,2].

To reduce the uses of OPC, the researches of the new cementitious materials have been studied. The geopolymer is new material and is suitable for replacing of PC in construction. The geopolymer can be using as cement-like gel binders with Al–O–Si bounds [3,4]. The Al or Si source can be obtained from the pozzolans as based material such as fly ash (FA), silica fume (SF), ground bottom ash (BA) and ground agricultural waste ashes (AWA). Various pozzolans are a variable in Thailand and in world. FA is the most common pozzolans and extensively used in the concrete industry worldwide [5–11]. However, the as-received industrial and agricultural by-product ashes are not yet good pozzolans materials and cannot be used directly. Therefore, the researches on the high performance of these pozzolans are as source material, needed to be developed by using the additive nanomaterials such as SiO2, Al_2O_3 and OPC [12–14].

On the other hand, the researchers are trying to improve the optical and electrical properties of cement and geopolymer by mixing with other materials such as TiO_2, ZnO, paraffin, $Pb(Ti,Zr)O_3$ (PZT), $BaTiO_3$ (BTO), $Ba_{0.85}Ca_{0.15}Ti_{0.9}Zr_{0.1}O3$ (BCTZO), and multi-walled carbon nanotubes (CNTs), etc., for application as smart materials in construction [15–25]. In particular, there has been increasing interest the applications of the TiO_2 as photocatalytic in concrete for air pollution remediation, self-cleaning and self-disinfection. It is expected that the photocatalytic coated buildings can maintain their aesthetic appearance and reduce urban air pollution level at the same time [15–17]. For electrical properties, there are many researches that reported using

multi-walled carbon nanotubes (CNTs) as an admixture in cement or concrete to improve electrical properties [20-23]. Han et al. [23] reported that the electrical resistance of the self-sensing CNT/cement composite is remarkably sensitive to compressive stress and reversible piezoresistive response. These findings indicate that this self-sensing nanocomposite cement has great potential for traffic-monitoring applications such as vehicle detection, weighing and speed measurement. Moreover, Zhang et al. [24] reported that cement-based piezoelectric composites are employed as the sensing elements of a new smart traffic monitoring system. The results indicate that the piezoelectricity of the cement-based piezoelectric sensors enables powerful and accurate real-time detection of the pressure induced by the traffic flow. However, the relationship between magnetic and mechanical properties of ferromagnetic $CoFe_2O_4$ nanopowders–cement and geopolymer composites for application in civil structure still have been studied.

Therefore, this research is interested in the improvement of the fabrication, electrical, magnetic and mechanical properties of the geopolymer by using ferromagnetic $CoFe_2O_4$ nanopowders composites. The $CoFe_2O_4$ nanopowders were prepared by precipitation method. The $CoFe_2O_4$ and geopolymer composite samples were fabricated by normal mixture method. The phase and microstructure of all samples were characterized by using XRD, FT-IR, TEM, SEM and XAS. The dielectric properties and magnetic properties are investigated. The relationships between the dielectric (magnetic) and mechanical properties of the composite samples are investigated.

2. Objectives

6.1 To synthesize the $CoFe_2O_4$ powders by co-precipitation method.

6.2 To fabricate the $CoFe_2O_4$ -geopolymer composites.

6.3 To characterize the structure, morphology, and valence electron of prepared $CoFe_2O_4$ and $CoFe_2O_4$-geopolymer composites by various techniques such as XRD, TEM, SEM, XPS, and XAS.

6.4 To study the dielectric, magnetic and mechanical properties of $CoFe_2O_4$ and $CoFe_2O_4$-geopolymer composites.

3. Methodology

The methodologies for this research are as follows:

3.1 Preparation of ferromagnetic $CoFe_2O_4$ nanopowders

The $CoFe_2O_4$ nanopowders are prepared by co-precipitation method. Firstly, the raw materials of Co and Fe chloride were dissolved in de-ionization. Secondly, the obtained solution was precipitated by NaOH solution to obtain the precursor powders. Then the precursor powder was calcined at 300, 500 and 700 ^{o}C to obtain the $CoFe_2O_4$ nanopowders.

3.2 Preparation of ferromagnetic $CoFe_2O_4$ nanopowders and geopolymer composites

The $CoFe_2O_4$ nanopowders were added to high calcium fly ash (FA) at the dosages of 0%, 1%, 3%, and 5% by weight. Constant liquid to binder (L/B) ratio of 0.50 and Na_2SiO_3/NaOH ratio of 1.0 were used in all mixtures. The mixing of pastes, NaOH and Na_2SiO_3 solutions were firstly mixed together and used as the liquid solution. For the FA and $CoFe_2O_4$ nanopowders were dry mixed until the mixture was homogenous. And then, the liquid solution was added and the mixing of pastes was done for 5 min. After mixing, paste specimens were molded in 25 mm diameter x 25 mm height plastic containers. They were wrapped with cling film and cured at 65 ^{o}C for 48 h.

3.3 Sample characterization

The crystal structure and phase formation of the prepared $CoFe_2O_4$ nanopowders are characterized by using x-ray diffraction (XRD), and transmission electron microscopy (TEM). Then, the morphologies and chemical compositions of the prepared samples are investigated by using scanning electron microscope (SEM). The valence states of various ions were determined by using X-ray photoelectron spectroscopy (XPS) X-ray absorption spectroscopy (XAS).

3.4 Study of dielectric, magnetic and mechanical properties of $CoFe_2O_4$ nanopowders and $CoFe_2O_4$-geopolymer composites

The electrical (dielectric and resistance) and magnetic properties are investigated. The relationships between the electrical and magnetic properties of composite samples are investigated. Moreover, the electrical, mechanical and magnetic properties of $CoFe_2O_4$ and $CoFe_2O_4$-geopolymer composite samples are compared with other literatures in cementitious composites.

4. Literature review

4.1 Geopolymer

The most common type of cement used by concrete manufacturers is ordinary Portland cement (OPC), which is prepared by igniting a mixture of raw materials mainly composed of calcium carbonate or aluminum silicates. OPC is defined as hydraulic cement produced by pulverizing clinker consisting essentially of hydraulic calcium silicates, usually containing one or more of the forms of calcium sulfate as an interground addition. The phase compositions in Portland cement Type I are shown in Table 1 and they are denoted as tricalcium silicate (C3S), dicalcium silicate (C2S), tricalcium aluminate (C3A), and tetracalcium aluminoferrite (C4AF).

Table 1 Components of Portland cement Type I

Description	Formula	% composition
tricalcium silicate (C3S)	$3CaO.SiO_2$	49
dicalcium silicate (C2S)	$2CaO.SiO_2$	25
tricalcium aluminate (C3A)	$3CaO.Al_2O_3$	12
tetracalcium aluminoferrite (C4AF)	$4CaO.Al_2O_3.Fe_2O_3$	8

Hydration is the reaction that takes place between cement and water that leads to setting and hardening. All compounds present in Portland cement clinker are anhydrous, but when brought into contact with water, they are all attacked or decomposed, forming hydrated compounds. When the tri- or di- calcium silicates react with water a calcium-silicate-hydrate gel is formed. This calcium-silicate hydrate (C-S-H) is the principal hydration product and primary binding phase in Portland cement. The chemical reactions that take place during hydration are summarized below (Figure 1).

Tricalcium silicate

$$2(3CaO.SiO_2)+6H_2O \longrightarrow 3CaO.2SiO_2.3H_2O+3Ca(OH)_2$$

Dicalcium silicate

$$2(2CaO.SiO_2)+4H_2O \longrightarrow 3CaO.2SiO_2.3H_2O +Ca(OH)_2$$

Tricalcium aluminate

$$3CaO.Al_2O_3+6H_2O \longrightarrow 3CaO.\ 2Al_2O_3.6H_2O$$

Tetracalcium aluminoferrite

$$4CaO.Al_2O_3.Fe_2O_3+2Ca(OH)_2+10H_2O \longrightarrow 3CaO.2Al_2O_3.6H_2O+3CaO.Fe_2O_3.H_2O$$

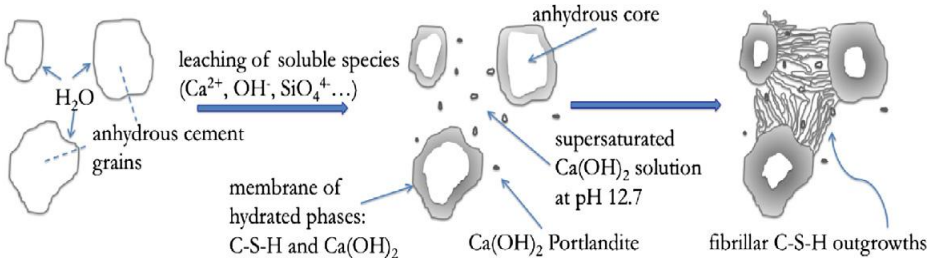

Figure 1 Schematic representation of the early stages of C3S hydration [28]

Geopolymer material is that of converting silicate and aluminosilicate form industrial wastes into strong and chemically durable cement-like gel binders, promising a new cement alternative in the field of construction materials. The term geopolymer was first found and invented by Davidovits which was obtained from fly ash as a result of geopolymerisation reaction. This was produced by the chemical reaction of alumino-silicate oxides (Si_2O_5–Al_2O_2) with alkali polysilicates yielding polymeric Si–O–Al bonds. The geopolymerization process involves three separate processes and during initial mixing, a clear representation of the reaction involved during the polymerization is explained in Figure 2.

First stage: “destruction–coagulation” This first disaggregation process entails the severance of the Me–O, Si–O–Si, Al–O–Al and Al–O–Si bonds in the starting material. Glukhovsky suggested that this disaggregation of the solid phase may be governed by the formation of complex unstable products whose origin lies in

the change in the ionic strength of the medium prompted by the addition of electron donor atoms (the alkaline metals). The result is a redistribution of the electronic density around the silicon atom, rendering the Si–O–Si bond more susceptible to rupture. The presence of alkaline metal cations neutralizes these anions, generating Si–O–Na^+ bonds, thereby hindering reaction reversibility. Moreover, the conditions created by the Si–O–Na^+ complexes, which are stable in alkaline media, are suitable for the transport of the reacting structural units and the development of the coagulated structure. Since the hydroxy groups have the same effect on the Al–O–Si bond, the aluminates in the alkaline solution form complexes such as $Al(OH)^{4-}$ or $Al(OH)_6^{3-}$, depending on the pH in the medium.

Second stage: “coagulation–condensation” In this second stage, accumulation enhances contact among the disaggregated products, forming a coagulated structure where polycondensation takes place. The polycondensation rate is determined by the state of the dissolved ions and the existence or otherwise of the conditions necessary for gel precipitation. Silicic acid condensation is therefore favoured at pH values in which the acid is slightly dissociated or in a molecular state. At pH~7, for instance, disaggregation of the Si–O–Si bond gives rise to $Si(OH)_4$-like hydroxylated complexes.

Third stage: “condensation–crystallization” The presence of particles from the initial solid phase, together with the appearance of microparticles resulting from condensation, favors product precipitation. The mineralogical composition of the initial phase, the nature of the alkaline component and the hardening conditions determine the qualitative and quantitative composition of the crystallized products.

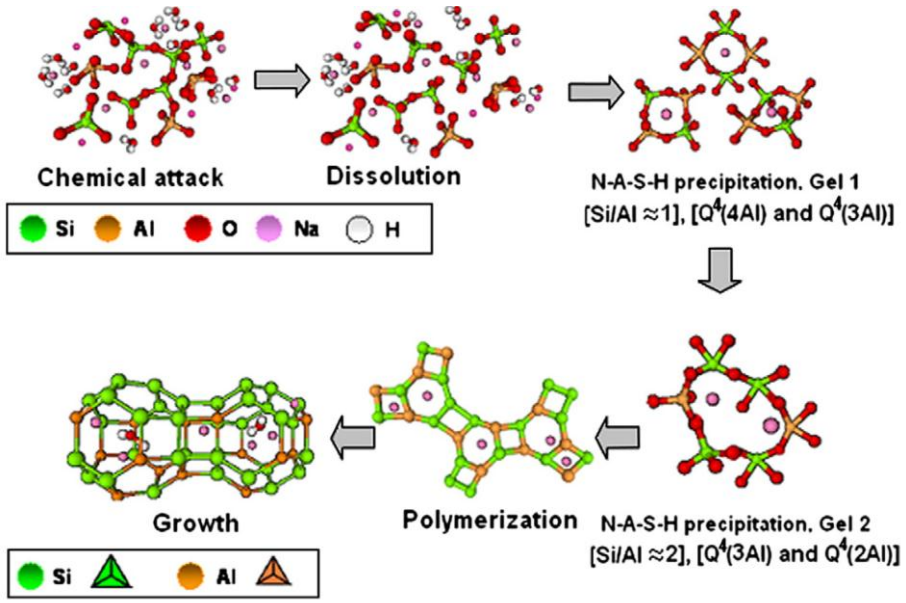

Figure 2 Descriptive model for alkali activation of aluminosilicates [29].

Cementinious geopolymer in Thailand has been reported by Prinya's group [5-12]. They studied the effect of composition and curing condition on mechanical properties by using fly ash, bottom ash, and rice husk ash as raw material. In particular, Rattanasak et al. [7] investigated the leaching of fly ash mixed with NaOH solution and on mixing procedure for preparing geopolymer (Figure 4). Leaching of SiO_2 and Al_2O_3 was investigated by mixing fly ash with NaOH solution for different time intervals and leachates were analyzed in terms of silica and alumina contents. To make geopolymer paste, separate mixing and normal mixing were used. For separate mixing, NaOH solution was mixed with fly ash for the first 10 min; subsequently sodium silicate solution was added into the mixture. For normal mixing, fly ash, sodium hydroxide and sodium silicate solution were incorporated and mixed at the same time. Geopolymers were cured at 65 $^{\circ}C$ for 48 h. Microstructure and compressive strength of mortar were investigated. Results revealed that solubility of fly ash depended on concentration of NaOH and duration of mixing with NaOH. For mixing procedure, separate mixing gave slightly better strength mortar than normal mixing. High strength geopolymer mortar up to 70.0 MPa was obtained

when the mixture was formulated with 10 M NaOH and sodium silicate to NaOH ratio of 1.0.

Table 2 Chemical composition (%) of fly ash from Mae Moh power plant in the north of Thailand [7].

SiO_2	Al_2O_3	CaO	Fe_2O_3	Na_2O	TiO_2	MgO	K_2O	P_2O_5	SO_3	LOI
39.5	19.5	17.3	14.1	1.3	0.5	2.3	2.9	0.2	2.6	0.8

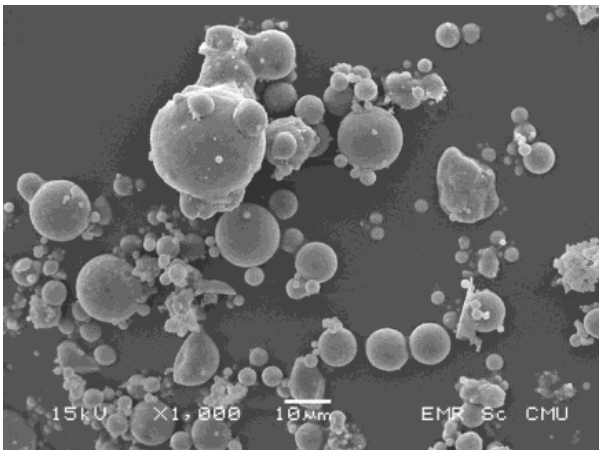

Figure 3 SEM image of fly ash from Mae Moh power plant in the north of Thailand.

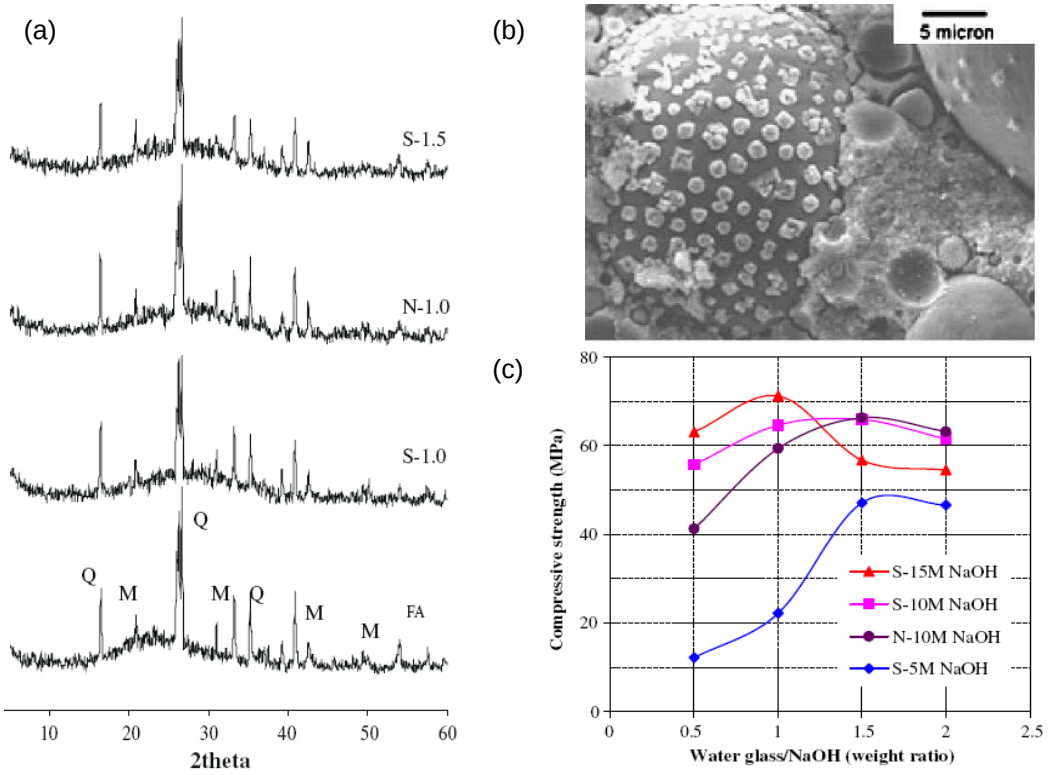

Figure 4 (a) XRD profiles of fly ash and geopolymer pastes: Q = quartz, M = mullite, (b) SEM micrograph of geopolymer, and (c) the relationship between water glass-to-NaOH ratio (G/N) and strength [7].

Moreover, the effect of adding nano-SiO_2 and nano-Al_2O_3 on the properties of high calcium fly ash geopolymer pastes were reported by Phoo-ngernkham et al. [12]. These nano-particles were added to fly ash at the dosages of 0%, 1%, 2%, and 3% by weight. The sodium hydroxide concentration of 10 molars, sodium silicate to sodium hydroxide weight ratio of 2.0, the alkaline liquid/binder ratio of 0.60 and curing at ambient temperature of 23 $^{\circ}$C were used in all mixtures. The results showed that the use of nano-SiO_2 as additive to fly ash results in the decrease of the setting time, while the addition of nano-Al_2O_3 results in only a slight reduction in setting time. Adding 1–2% nano-particles could improve compressive strength, flexural strength, and elastic modulus of pastes due to the formation of additional calcium silicate hydrate (CSH) or calcium aluminosilicate hydrate (CASH) and sodium aluminosilicate hydrate (NASH) or geopolymer gel in geopolymer matrix.

In addition, the additions of both nano-SiO_2 and nano-Al_2O_3 enhance the shear bond strength between concrete substrate and geopolymer.

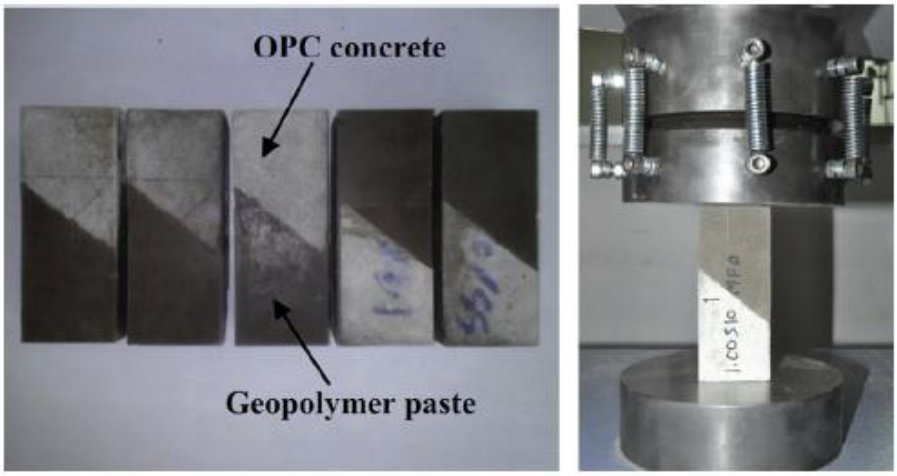

Figure 5 Slant shear specimens (a) and testing procedure (b) [12].

4.2 Cement (geopolymer)–electrical material composites

Cement-based electrical material composites is the most popularly studied for the development of the smart or intelligent structures in civil engineering such as store thermal energy, health monitoring of structures and active vibration control of structures [15-27].

Han et al. [22] reported the phase change materials (PCM) incorporated with cementitious construction materials to store thermal energy and control interior climate in buildings, which can reduce the energy consumption and improve thermal comfort. The addition of PCM is found to decrease strength and thermal conductivity of the cement-based composite. Therefore, carbon nanotubes (CNT) are integrated into cementitious construction materials with microencapsulated PCM to improve their thermal-conductive and mechanical performances. Results of lab and outdoor tests show the modified cement mortar containing both PCM and CNT exhibits better heat insulation properties than plain cement mortar. A temperature difference up to 6.8 $^{\circ}C$ was observed between interiors of two same size scale-down building models

(one made of plain cement mortar, the other one made of cement mortar with PCM and CNT) (Figure 6). This indicates that the modified cement mortar can effectively enhance the thermal storage property of cement-based building materials.

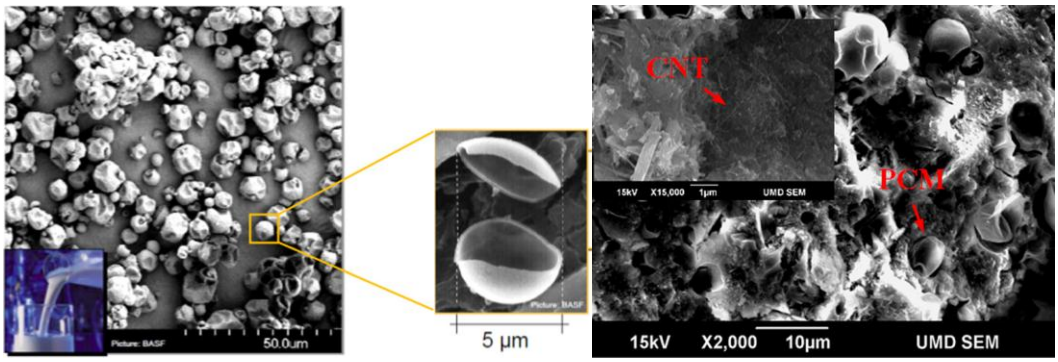

Figure 6 (a) Photographs of Micronal® DS 5000X, (b) SEM photographs of PCM/cement mortars with CNT: (5% PCM and 1% CNT) [22].

The self-sensing carbon nanotube (CNT)/cement composites, for traffic flow measurement, by detecting the change of electrical resistance of the composite when subject to the stress of a vehicle [25, 27-35]. Being an integral part of the pavement with strong mechanical strength, this new traffic sensor will provide several advantages over the inductive loop detectors, such as easy installation and maintenance, long service life with low maintenance cost, wide detection area, and potential applications for weigh-in-motion measurement. The field of nanotechnology is rapidly maturing into a fertile and interdisciplinary research area from which new smart materials can be developed. Carbon nanotubes (CNTs) have been widely used for a variety of applications due to their excellent physical properties, high strength and Young's modulus (the tensile strength and Young's modulus of CNTs are 20 times and 10 times those of carbon fibers (CFs) respectively), large deformation and high ductility (the elongation at breaking of CNTs is 18%, and is 18 times that of CFs), large force of bonding with the matrix (the inter-laminar shear strength of CNT/epoxy composites is 10 times that of CF/epoxy composites), high aspect ratio (>500), and excellent electrical conductivity. In particular, the

extremely high aspect ratio and low density of CNTs makes them easy to form into a conductive network and reinforcement network with a doping level as low as 0.1 wt% of CNTs [30-32]. CNTs also have interesting electromechanical properties. When subjected to stress/strain, the CNTs will show electrical properties that change with the level of stress/strain, expressing a linear and reversible piezoresistive response (the electromechanical properties of CFs were irreversible due to the fiber breakage when the strain was larger than 0.2%) [33-35]. Because the properties of CNTs are superior to those of CFs, it looks promising to develop smart concrete with excellent piezoresistivity by using CNTs as an admixture (Figure 7 and 8).

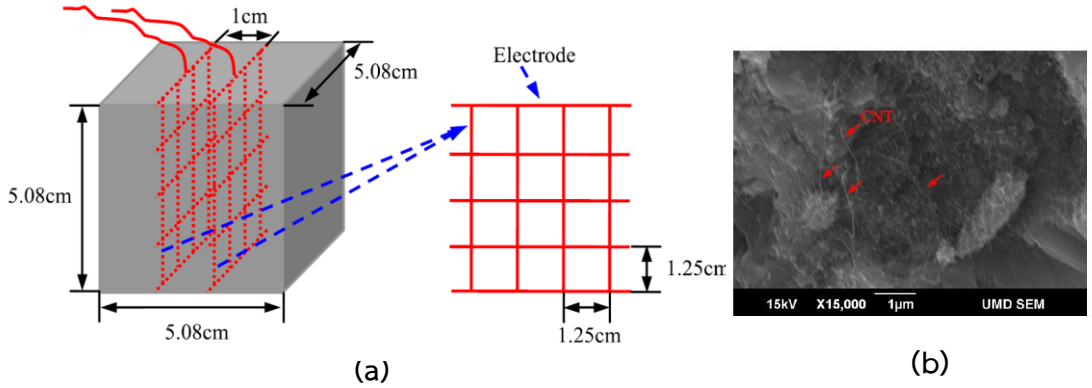

Figure 7 (a) Structure of the self-sensing CNT/cement composite specimen and arrangements of electrodes, and (b) SEM photograph of CNT concrete [25].

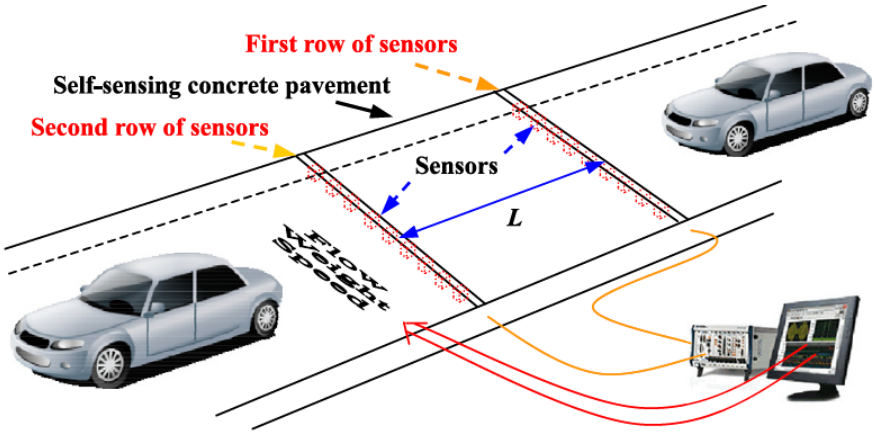

Figure 8 Illustration of self-sensing concrete pavement for traffic flow direction [25].

Zhang et al. [26] reported that cement-based piezoelectric composites are employed as the sensing elements of a new smart traffic monitoring system (Figure 9). The piezoelectricity of the cement-based piezoelectric sensors enables powerful and accurate real-time detection of the pressure induced by the traffic flow. To describe the mechanical-electrical conversion mechanism between traffic flow and the electrical output of the embedded piezoelectric sensors, a mathematical model is established based on Duhamel's integral, the constitutive law and the charge-leakage characteristics of the piezoelectric composite. From the laboratory tests show that the voltage magnitude of the sensor is linearly proportional to the applied pressure, which ensures the reliability of the cement-based piezoelectric sensors for traffic monitoring. A series of on-site road tests by a 10 tonne truck and a 6.8 tonne van show that vehicle weight-in-motion can be predicted based on the mechanical electrical model by taking into account the vehicle speed and the charge-leakage property of the piezoelectric sensor. In the speed range from 20 km/h to 70 km/h, the error of the repeated weigh-in-motion measurements of the 6.8 tonne van is less than 1 tonne. The results indicate that the embedded cement-based piezoelectric sensors and associated measurement setup have good capability of smart traffic monitoring, such as traffic flow detection, vehicle speed detection and weigh-in-motion measurement.

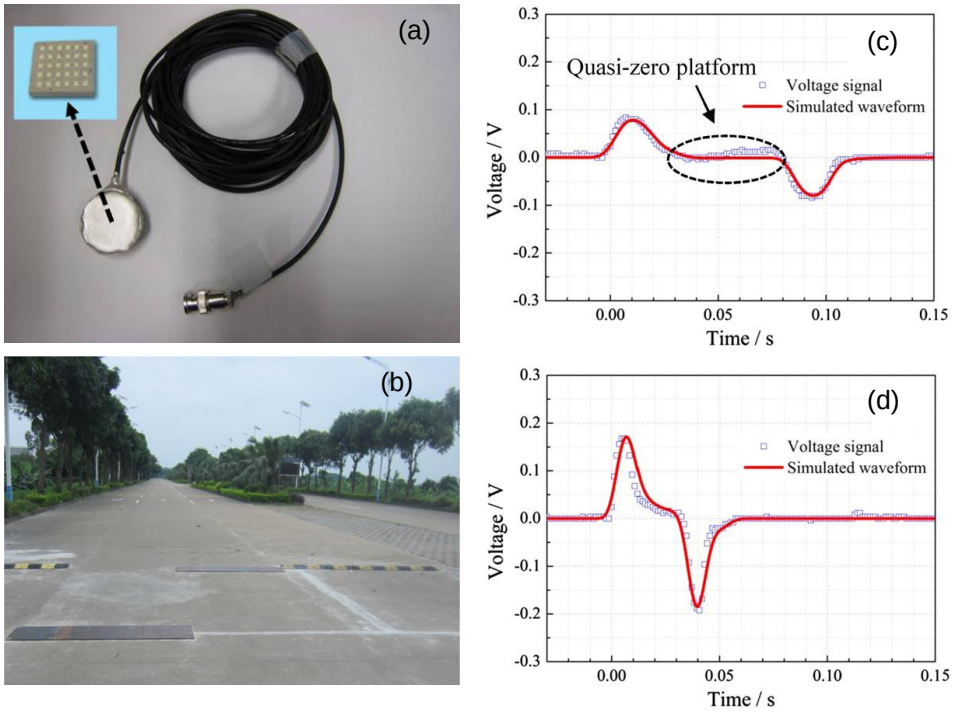

Figure 9 (a) Piezoelectric sensor with cement-based composite patch inside, (b) setup of the smart traffic monitoring system, and the voltage signals and simulated waveforms of the second weigh-beam by the front axle of the 10t truck at different velocities. (c) 20 km/h and (d) 60 km/h [26].

Saafi et al. [27] reported the reduction of graphene oxide during the processing of fly ash-based geopolymers offers a completely new way of developing low-cost multifunctional materials with significantly improved mechanical and electrical properties for civil engineering applications such as bridges, buildings and roads. In this paper, we present for the first time the self-sensing capabilities of fly ash-based geopolymeric composites containing in situ reduced graphene oxide (rGO). Geopolymeric composites with rGO concentrations of 0.0, 0.1 and 0.35% by weight were prepared and their morphology and conductivity were determined. The piezoresistive effect of the rGO-geopolymeric composites was also determined under tension and compression. The Fourier transform infrared spectroscopy (FTIR) results indicate that the rGO sheets can easily be reduced during synthesis of geopolymers due to the effect of the alkaline solution on the functional groups of GO. The

scanning electron microscope images showed that the majority of pores and voids within the geopolymers were significantly reduced due to the addition of rGO. The rGO increased the electrical conductivity of the fly ash-based rGOgeopolymeric composites from 0.77 S/m at 0.0 wt% to 2.38 S/m at 0.35 wt%. The rGO also increased the gauge factor by as much as 112% and 103% for samples subjected to tension and compression, respectively.

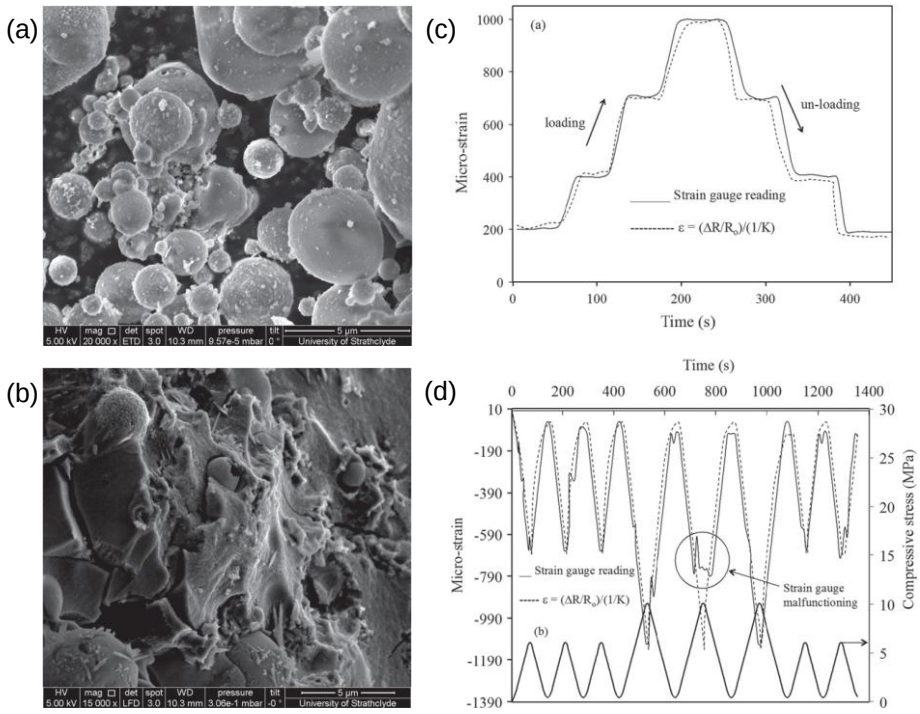

Figure 10 (a) SEM image of FA particles used in this investigation, (b) morphology of rGO-geopolymeric composites with 0.35 wt%., and the response of rGO-geopolymeric composites under loading-unloading and cyclic stress (c) tension and (d) compression [27].

Moreover, the need of preventing electromagnetic interference (EMI) has been increasing with the development and application of electronic science and communication technology [36]. EMI prevention is particularly needed for underground vaults containing transformers and other electronics that are related to electric power and telecommunication [37]. Electronic radiation has been a threat to the public health and has brought out information leakage. Thus, the capacity of a

building to prevent the electromagnetic radiation or electromagnetic interference is very important.

Li et al. [38] reported the magnetic composites of barium ferrite coated on fly-ash cenospheres (BFACs) were prepared by sol–gel auto-combustion method. To promote surface activity, they modified fly-ash cenospheres (FACs) surfaces using c-aminopropyltriethoxysilane (APS) as coupling agent and silver nitrate as activating agent before coating barium ferrite films on FACs. Continuous and uniform coatings of barium ferrite were found on the surfaces of the FACs. The BFACs powders-epoxy composite possesses excellent microwave absorption properties in the 2–18 GHz frequency range. The maximum microwave reflection loss reaches 15.4 dB at 8.4 GHz with a thickness of 3.0 mm, and the widest bandwidth less than 12 dB is 6.2 GHz with a sample thickness of 2.0 mm (Figure 11). The intrinsic reasons for microwave absorption were also investigated. Applications of this composite material in magnetic recording, electromagnetic wave shielding and lightweight microwave-absorbing fields are promising.

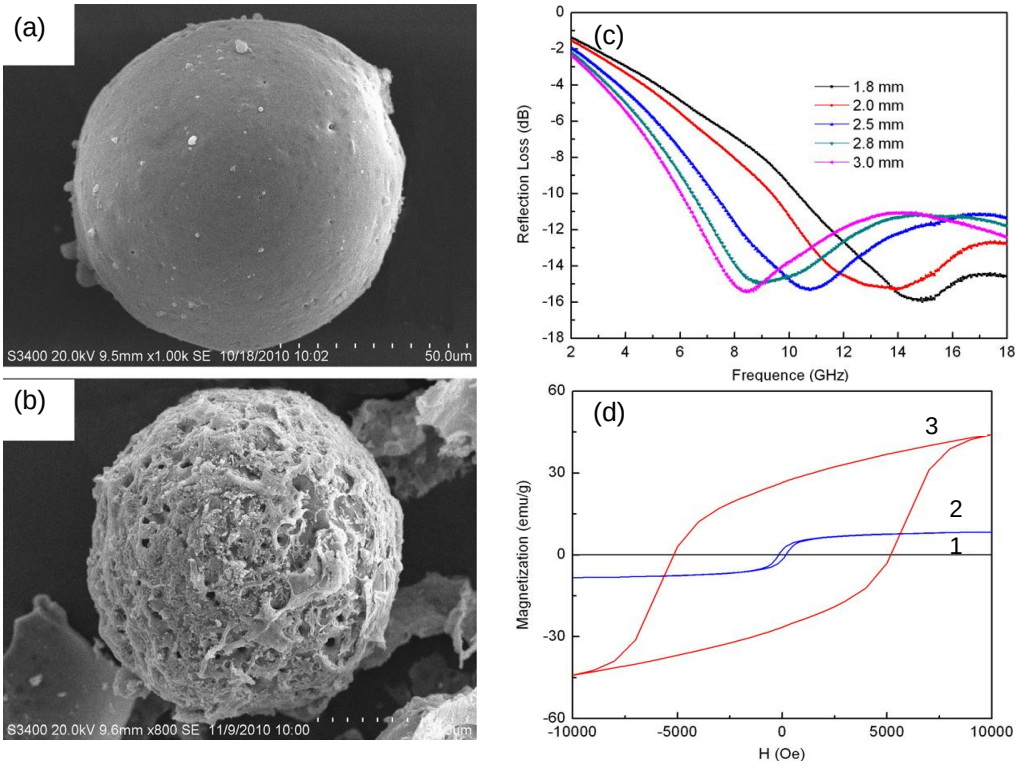

Figure 11 SEM images of (a) pristine FAC, (b) the composite powder of BFAC, (c) dependence of reflection loss on frequency for composite powders with various thickness, and (d) Magnetization hysteresis loops for (1) pristine FACs; (2) as-burned powders; and (2) the composite powders of BFACs [36].

Moreover, the spinel MFe_2O_4 (M= Co, Mn, Ni, Zn, and Cu etc.) ferrite is one of the magnetic materials which are interesting for composite with cementitious materials due to a wide range of applications including microwave absorption, ferrofluids, catalysis, etc [39-43]. Spinel ferrites present a spinel-type structure (Fd3m) in which the O^{2-} ions are arranged in a cubic with close packing being occupied one-eighth of tetrahedral (A) and one-half of octahedral (B) interstitial sites (Figure 12). Among these spinel ferrites, the cobalt ferrite ($CoFe_2O_4$) has been investing due to a wide range of applications including electronic devices, ferrofluids, magnetic delivery microwave devices and high density information storage. Moreover, $CoFe_2O_4$ has the high magneto-striction, high rate of change of strain with magnetic field, cubic magneto-crystalline anisotropy, high coercivity, moderate saturation magnetization,

high Curie temperature TC, high chemical stability and good electrical insulation [42,43].

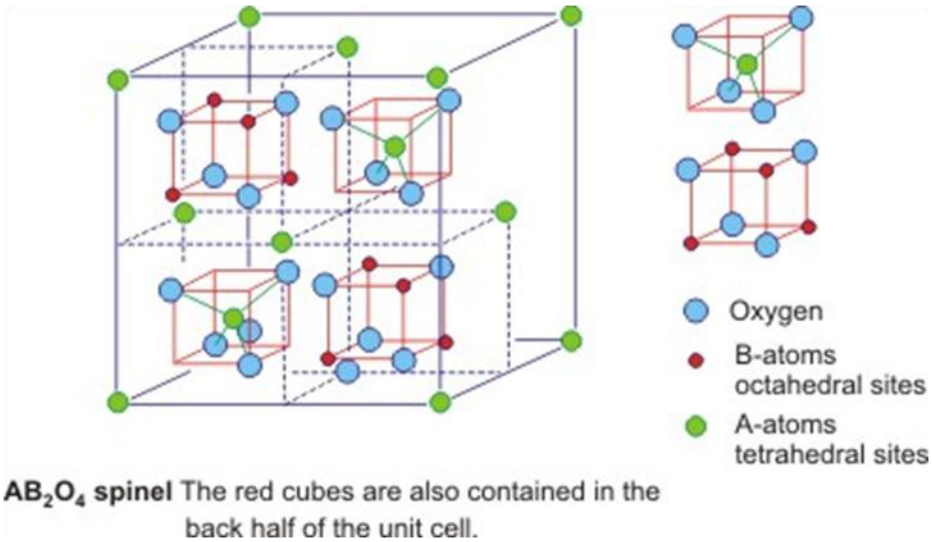

Figure 12 Structure of spinel ferrite [44].

Recently, many synthetic methodologies have been utilized to produce magnetic nanostructures including co-precipitation [44-46], combustion [47], hydrothermal or solvothermal synthesis [48-50], and electrospinning [51-53] etc. Among these synthesis techniques, precipitation or co-precipitation is a simple and low cost method (Table 4). The obtained powders have high magnetization and coercivity field when compared with other methods as shown in Table 3. The diameters of obtained powders are in the ranging of nanometers (Figure. 13).

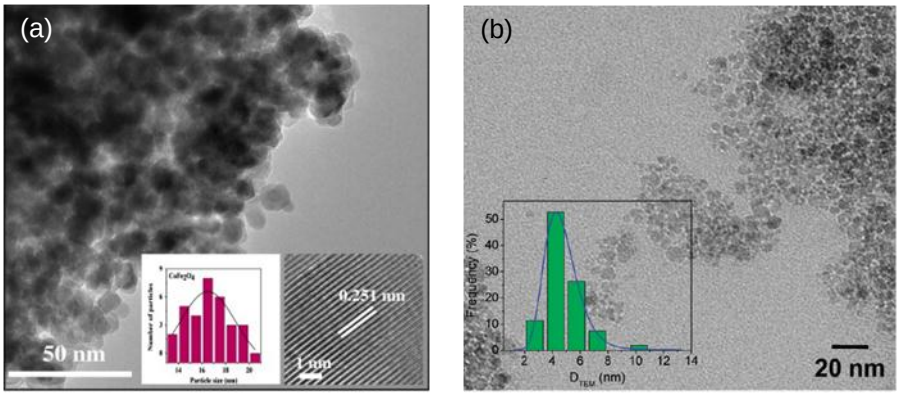

Figure 13 $CoFe_2O_4$ powders prepared by co-precipitation method (a) NaOH as precipitation agent [45] and (b) alkanolamines isopropanolamine (MIPA) and diisopropanolamine (DIPA) as precipitation agent [46]

Table 3 Magnetization properties of some spinel ferrite powders prepared by different method

Samples	Method	Particle size (nm)	Saturation Magnetization (emu/g)	Coercivity field (Oe)	References
$NiFe_2O_4$	Sol-gel	40.5	43.5	124.5	[55]
	Solvothermal	7.1	39.5	-	[50]
$ZnFe_2O_4$	Hydrothermal	17	7	9.8	[49]
	Modified sol-gel	100	1.5	47	[54]
$MnFe_2O_4$	Solvothermal	7.4	53.5	-	[50]
	Hydrothermal	13.8	28.4	46.5	[48]
$CoFe_2O_4$	Combustion	43	68.4	483	[47]
	Co-precipitation	15	69.6	775	[45]
	Hydrothermal	6-10	55	74	[48]
	Solvothermal	8.9	58.4	-	[50]
	Electrospinning	175	42	611	[53]

Table 4 Comparing the advantage and disadvantage of different method for the preparing $CoFe_2O_4$ nanopowders

Method	advantage	disadvantage	References
Combustion	-high temperature (500-800°C) -high amount of the obtained product per times	-high cost of raw materials	[47]
Co-precipitation	-low to high temperature (100-800 $^{\circ}$C) -high amount of the obtained product per times -low cost of raw materials	-	[45]
Hydrothermal	-low temperature (100-200 $^{\circ}$C) -low cost of raw materials	-low amount of the obtained product per times	[48]
solvothermal	-low temperature (100-200 $^{\circ}$C)	-low amount of the obtained product per times -low cost of raw materials	[50]
electrospinning	-high temperature (600-800°C) -high cost of raw materials	-low amount of the obtained product per times	[53]

5. Results and Discussion

5.1 The XRD study of $CoFe_2O_4$ nanopowders

The $CoFe_2O_4$ nanopowders are prepared by co-precipitation method. Firstly, the raw materials of Co and Fe nitrate were dissolved in de-ionization. Secondly, the obtained solution was precipitated by NaOH solution to obtain the precursor powders. Then the precursor powder was calcined at difference temperature to obtain the $CoFe_2O_4$ nanopowders. The structure of the synthesized $CoFe_2O_4$ was determined from the XRD patterns shown in Figures 14(a), 14(b) and 15(a) for $CoFe_2O_4$ nanoparticles synthesized at pH values of 9, 11 and 14 respectively. Within each of these Figures are shown the spectra obtained from samples calcined at temperatures of 300, 500 and 700°C for 1 h in air for each of the pH concentrations employed during synthesis. The peaks in each sample matched the (111), (220), (311), (222), (400), (422), (511), and (440) reflections associated with the spinel cubic structure of $CoFe_2O_4$ according to the JCPDS standard 22-1086. Samples prepared at a pH of 9 and calcined at temperatures of 500 and 700°C (Figure. 14(a)) exhibited an impurity phase which could be associated with Fe_2O_3 (JCPDS 20-1099) and the peak positions associated with this phase are shown by the lower sets of vertical lines along the horizontal axes. The average crystallite sizes (*D*) of $CoFe_2O_4$ nanoparticles were calculated using Scherrer's equation or $D = 0.89\lambda/(\beta\cos\theta)$ where λ is the wavelength of the X-ray radiation used, β is the full width at half maximum (FWHM) and θ is the diffraction angle [18]. The values of *D* were mostly increasing with increasing calcination temperature for each pH value and were in the range between ~7 and ~47 nm as shown in Figure 15(b). The effect of increasing calcination temperature for all pH values is that the lattice constants as determined from the peak positions increased in the range between 8.342 and 8.400 Å (as shown in Figure 15(b) and Table 5) in general agreement with JCPDS 22-1086. This can be attributed due to grain growth and densification of the crystal [19]. The lattice constants tend to increase with the calcination temperature which was been reported by others [20,21]. However the lattice constants measured from the

samples with pH14 are not increasing monotonically with calcination temperature as has also reported by others [22, 23]. These results may be due to the defect structure in lattices changing with the increasing calcination temperature.

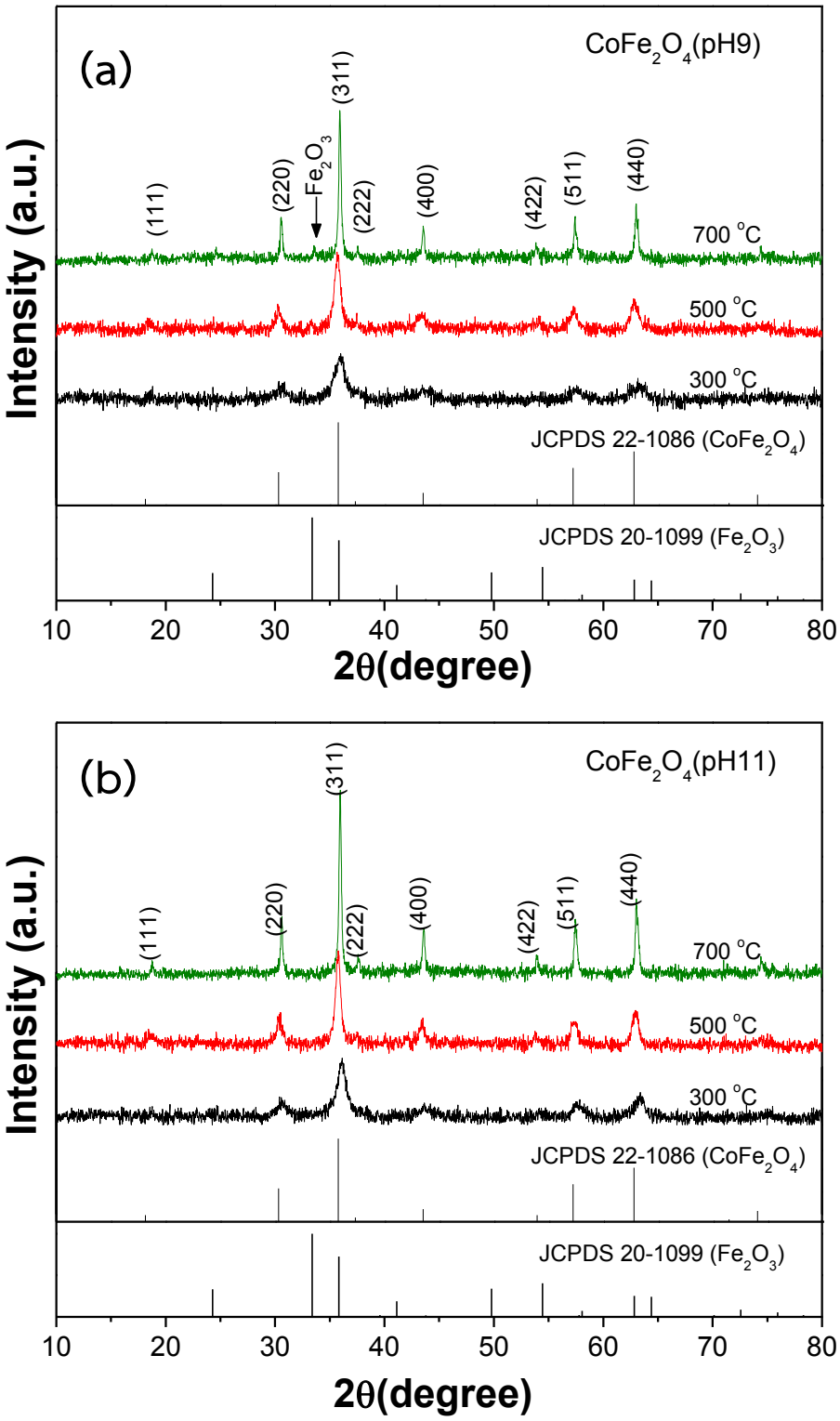

Figure 14 XRD patterns obtained from $CoFe_2O_4$ samples calcined at various temperatures and synthesized at pH values of (a) 9 and (b) 11.

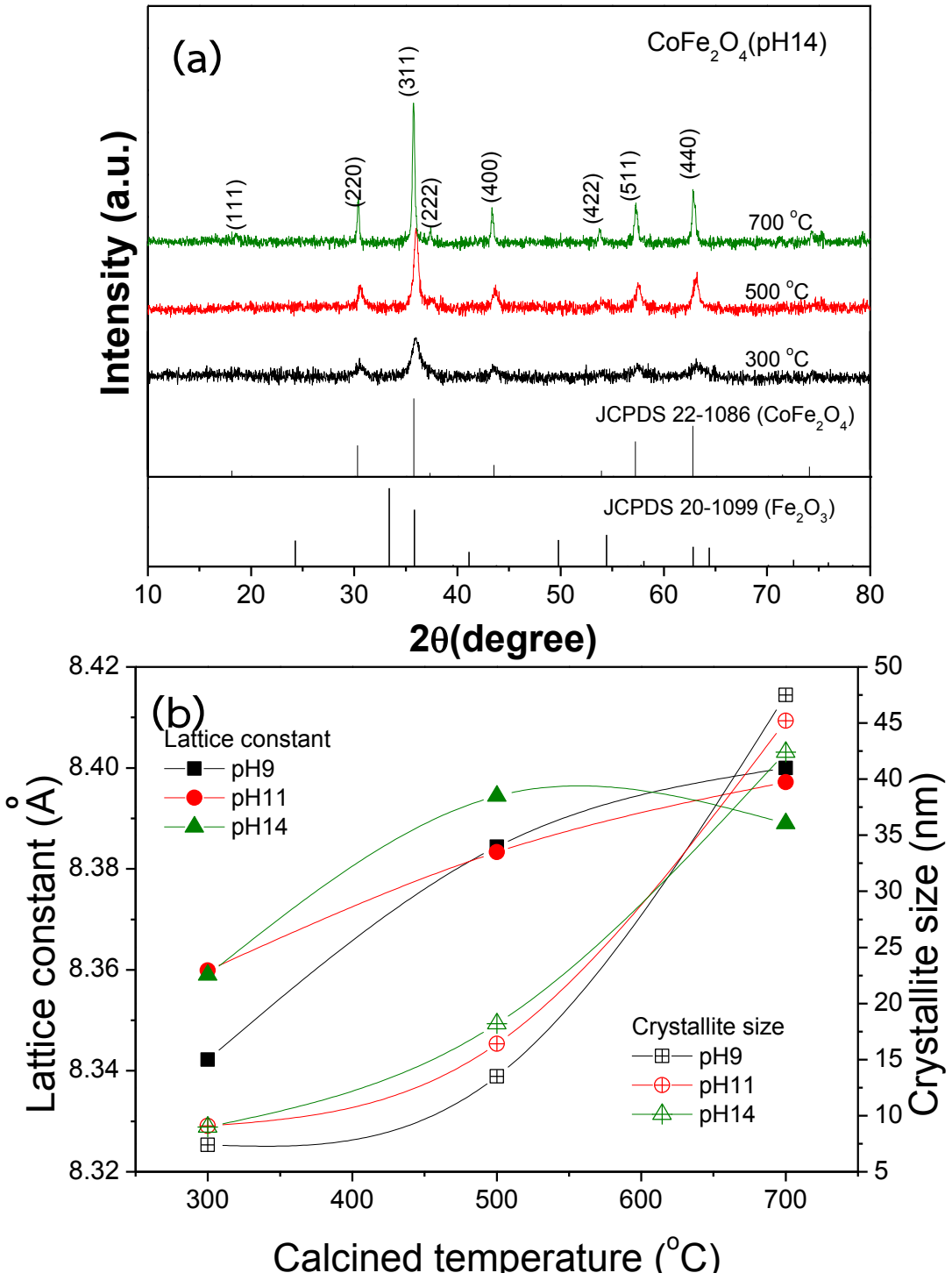

Figure 15 XRD patterns obtained from $CoFe_2O_4$ samples calcined at various temperatures and synthesized at pH values of (a) 14, and (b) shows average crystallite sizes and lattice constants as determined from the XRD spectra.

Table 5 Average crystallite sizes and lattice constants as determined from the XRD spectra.

Samples		Crystallite size (nm)	lattice parameter (Å)
pH9	300	7.7	8.343
	500	13.4	8.385
	700	42.3	8.400
pH11	300	9.1	8.360
	500	16.5	8.383
	700	44.1	8.397
pH14	300	8.6	8.343
	500	17.5	8.385
	700	38.1	8.400

5.2 The XAS study of valence states of Co and Fe in the $CoFe_2O_4$ samples

The valence states of Co and Fe in the $CoFe_2O_4$ samples prepared for all pH values and calcined at 700^{o}C were determined from XANES measurements made in transmission mode at room temperature in the vicinity of the Co and Fe K absorption edges as shown in Figures 16 (a, b) and 17 (a, b) respectively. These Figures show the edge energies of various Co and Fe standards as well as the samples to allow a comparison to be made. From the XANES results, the edge positions for all samples were close to those of the CoO (Co^{2+}) and Fe_2O_3 (Fe^{3+}) standards, indicating that these were the valence states of most of the Co and Fe ions

.

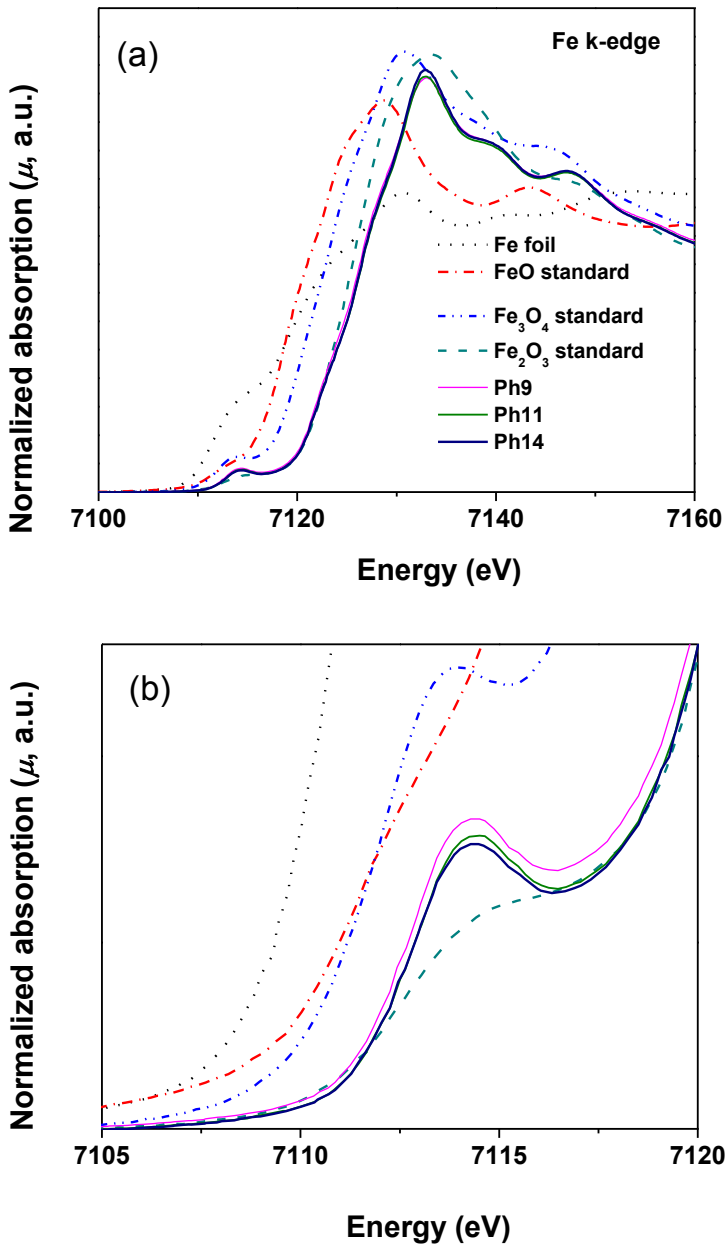

Figure 16 (a) XANES spectra in the vicinity of the Fe K absorption edges obtained from Fe foil, FeO (Fe^{2+}), Fe_3O_4 (Fe^{2+}, Fe^{3+}) and Fe_2O_3 (Fe^{3+}) standards and from the $CoFe_2O_4$ samples which were calcined at 700°C, and (b) an enlarged view pre-edges of XANE spectra.

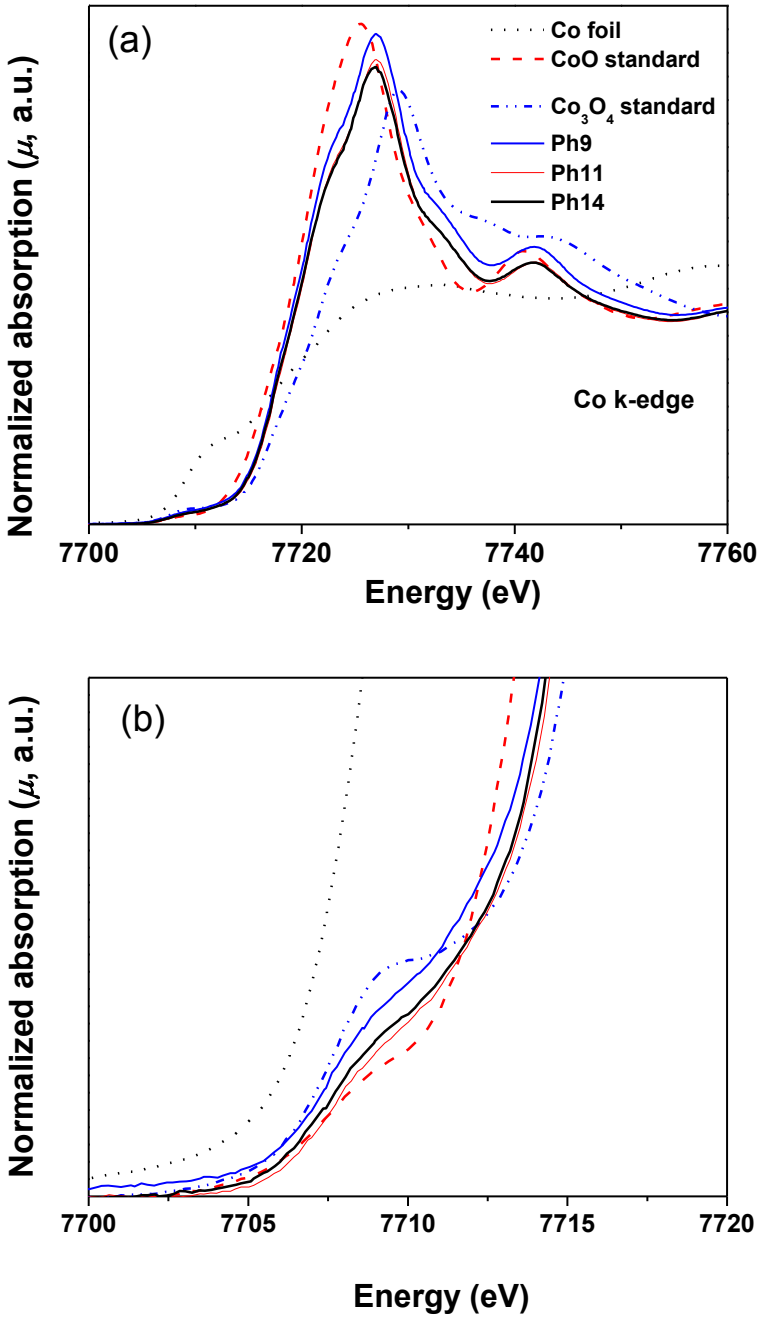

Figure 17 (a) XANES spectra in the vicinity of the Co K absorption edges obtained from Co foil, CoO (Co^{2+}) and Co_3O_4 (Co^{2+}, Co^{3+}) standards and from the $CoFe_2O_4$ samples which were calcined at 700°C, and (b) an enlarged view pre-edges of XANE spectra.

5.3 The XPS study of valence states of Co and Fe in the $CoFe_2O_4$ samples

XPS measurements were carried out to investigate the electronic state. The high resolution Co $2p_{3/2}$ spectra of pH9, pH11, and pH14 is associated with two spin-orbit characteristics of $Co2p_{3/2}$, and $Co2p_{1/2}$ as shown in Fig. 18(a)-20(a). The Co 2p and Fe 2p spectra are deconvoluted for the quantitative analyses. In high resolution Co 2p spectra, the two peaks assigned at ~796 eV and ~780 eV are demonstrating that Co is in 2+ state [14]. Deconvolution of the Co $2p_{3/2}$ peak regions of the pH9, pH11, and pH14 reveals the presence of two non equivalent bonds due to octahedral and tetrahedral lattice sites [16]. The binding energies of the all peaks along with the corresponding area under the curves of pH9, pH11, and pH14 are enlisted in Table 6. The binding energy of pH9 at 780.66 eV reveals that Co^{2+} have octahedral bonding with oxygen where as binding energy at 782.72 eV is due to the tetrahedral bonding of Co^{2+} with oxygen ions [27]. The peaks situated at 780.51 eV and 782.67 eV are attributed to Co^{2+} in octahedral and tetrahedral sites of the samples. The peaks assigned at 780.42 eV and 782.71 eV are related to the octahedral and tetrahedral sites of samples. XPS spectra of pH9, pH11, and pH14 of Co^{2+} show satellite peaks at the high binding energy side of both $2p_{3/2}$ and $2p_{1/2}$ regions, indicating that Co is in 2+ oxidation state [14]. Moreover, Fig. 18(b)-20(b) shows high resolution Fe 2p spectra of pH9, pH11, and pH14 that are associated with two spin-orbit characteristics of Fe $2p_{3/2}$, and Fe $2p_{1/2}$, respectively. The peak situated at ~711eV ($2p_{3/2}$) and ~724 eV ($2p_{1/2}$) indicates that Fe is in 3+ state [14]. The binding energies associated with Fe $2p_{3/2}$ and Fe $2p_{1/2}$ for pH9, pH11, and pH14 are enlisted in Table 6.

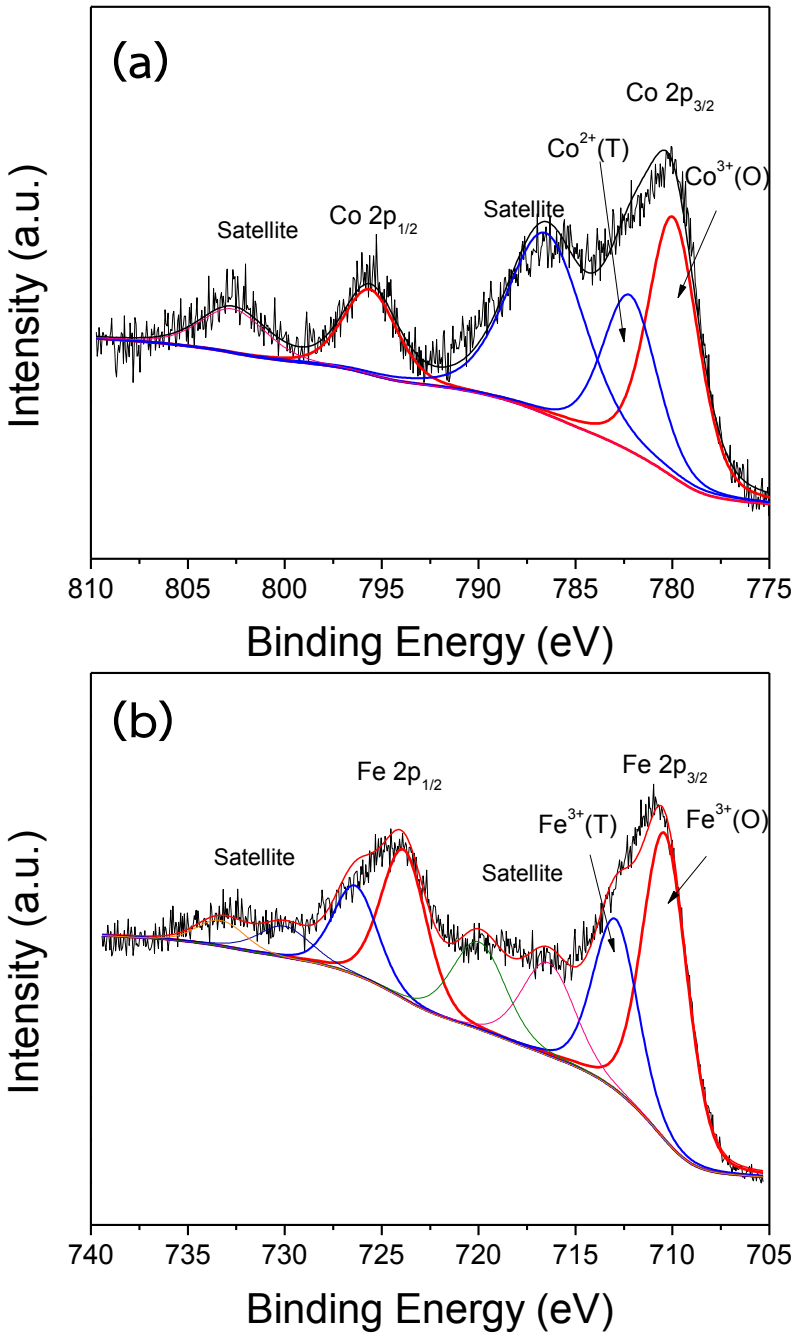

Figure 18 High-resolution deconvoluted XPS spectra of (a) Co 2p, and (b) Fe 2p of the $CoFe_2O_4$ samples were calcined at 700°C with pH values of 9

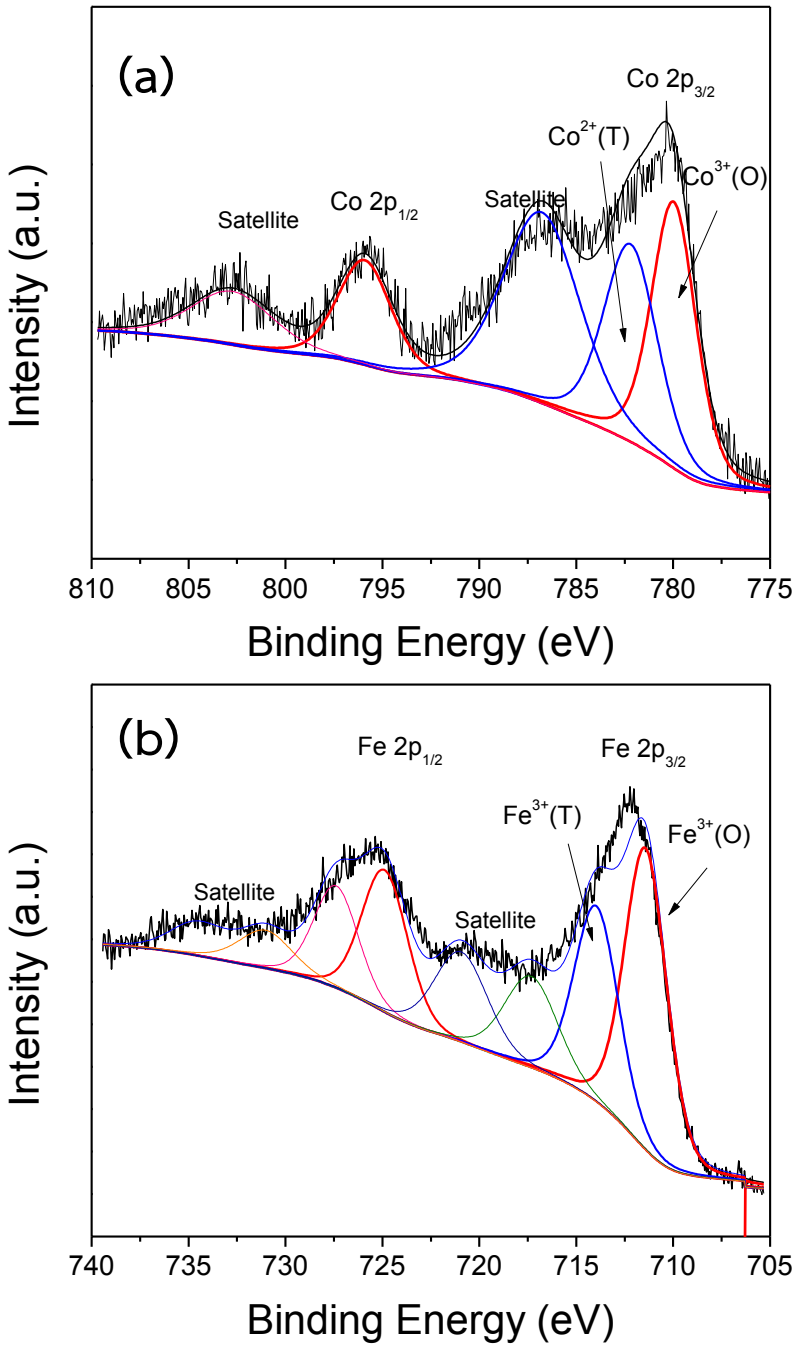

Figure 19 High-resolution deconvoluted XPS spectra of (a) Co 2p, and (b) Fe 2p of the $CoFe_2O_4$ samples were calcined at 700°C with pH values of 11

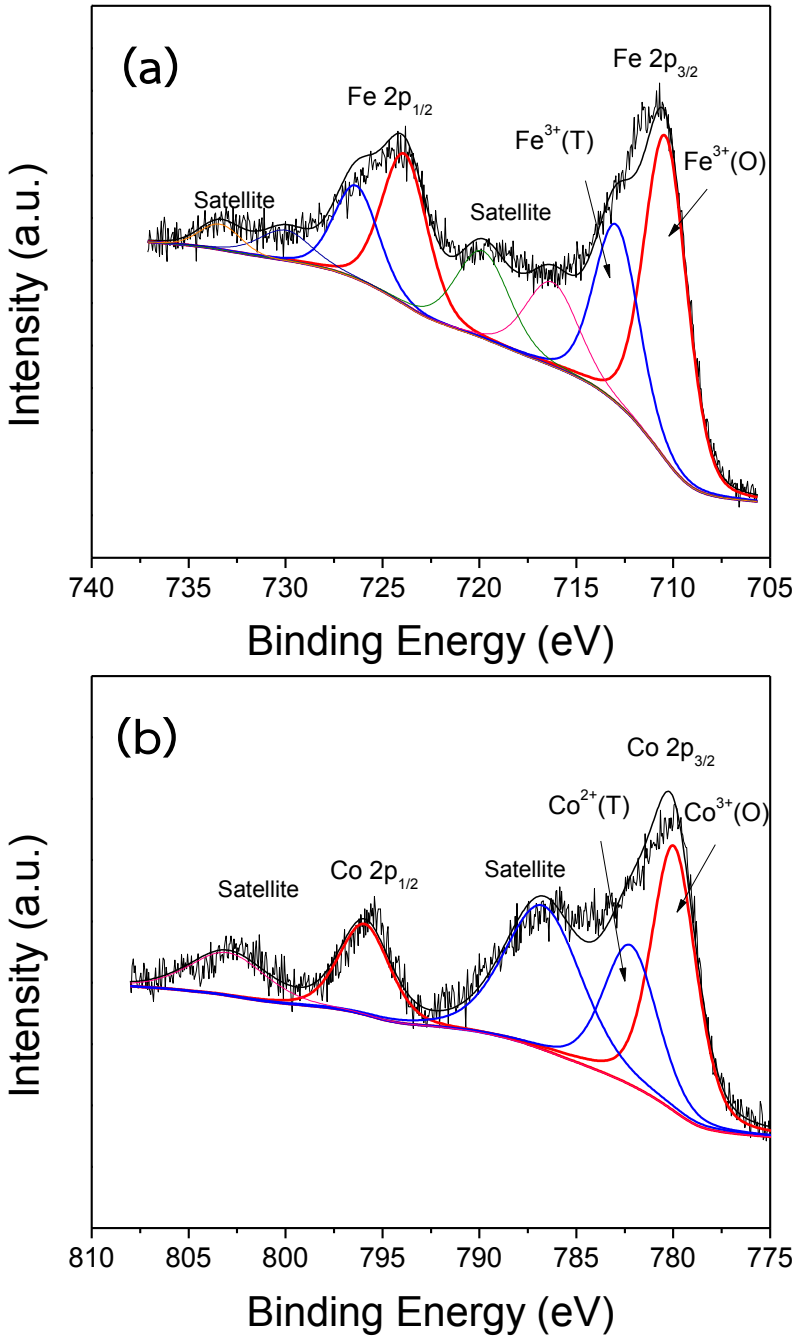

Figure 20 High-resolution deconvoluted XPS spectra of (a) Co 2p, and (b) Fe 2p of the $CoFe_2O_4$ samples were calcined at 700°C with pH values of 14

Table 6 Binding energy positions of the $CoFe_2O_4$ samples were calcined at 700°C with pH values of 9, 11 and 14.

Samples		Co 2p3/2	Fe 2p3/2
pH9	300	7.7	8.343
	500	13.4	8.385
	700	13.4	8.385
pH11	300	9.1	8.360
	500	16.5	8.383
	700	44.1	8.397
pH14	300	8.6	8.343
	500	17.5	8.385
	700	38.1	8.400

5.4 The TEM study of morphology of the $CoFe_2O_4$ samples

Figures 21-23 show the morphology, average particle sizes and structures of the $CoFe_2O_4$ nanoparticles for samples prepared at pH values of 9, 11 and 14 respectively. The morphology and particle size histograms were obtained from TEM bright field images and showed irregular shaped aggregated particles for each pH concentration with particle sizes increasing with increasing calcination temperature. It can be seen from the histograms that the average particle sizes of the samples were in the range from ~10 to ~38 nm which is consistent with the XRD results. The selected area electron diffraction (SAED) patterns obtained from all samples exhibited the spotty ring patterns typical of polycrystalline materials.

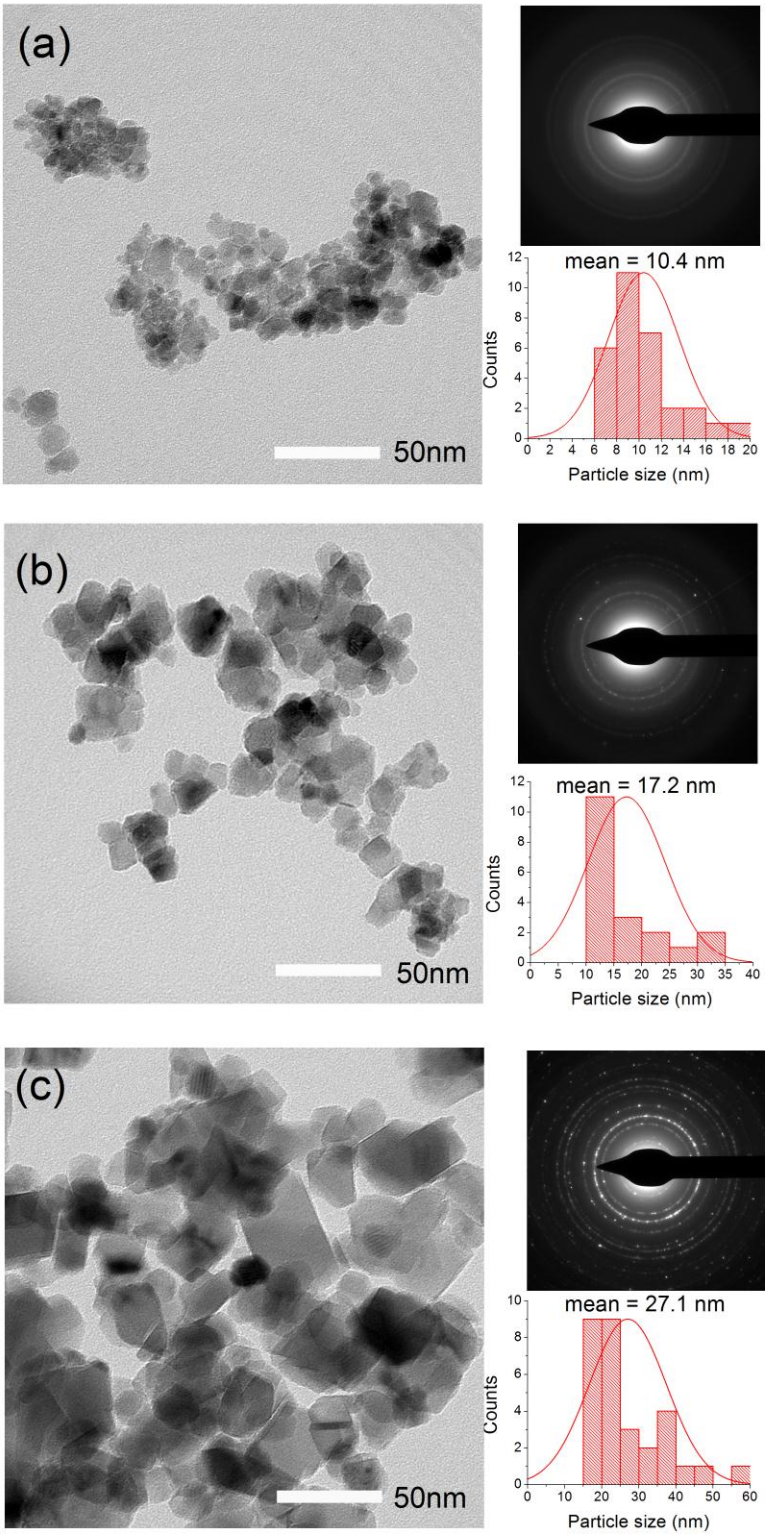

Figure 21 TEM images with selected-area electron diffraction (SAED) patterns and particle size histograms obtained from $CoFe_2O_4$ samples prepared at a pH of 9 and calcined at (a) 300°C (b) 500°C and (c) 700°C.

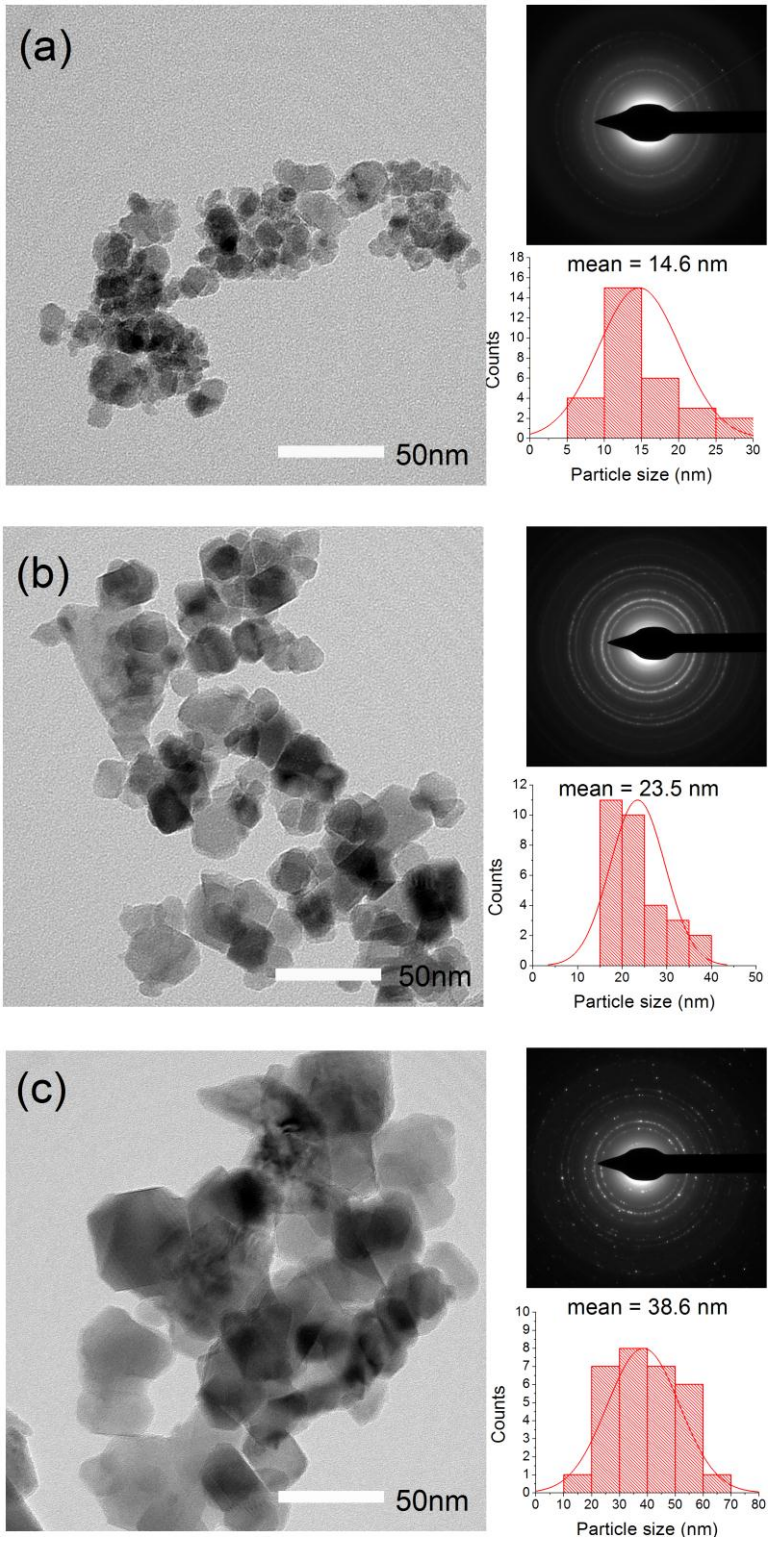

Figure 22 TEM images with selected-area electron diffraction (SAED) patterns and particle size histograms obtained from $CoFe_2O_4$ samples prepared at a pH of 11 and calcined at (a) 300°C (b) 500°C and (c) 700°C.

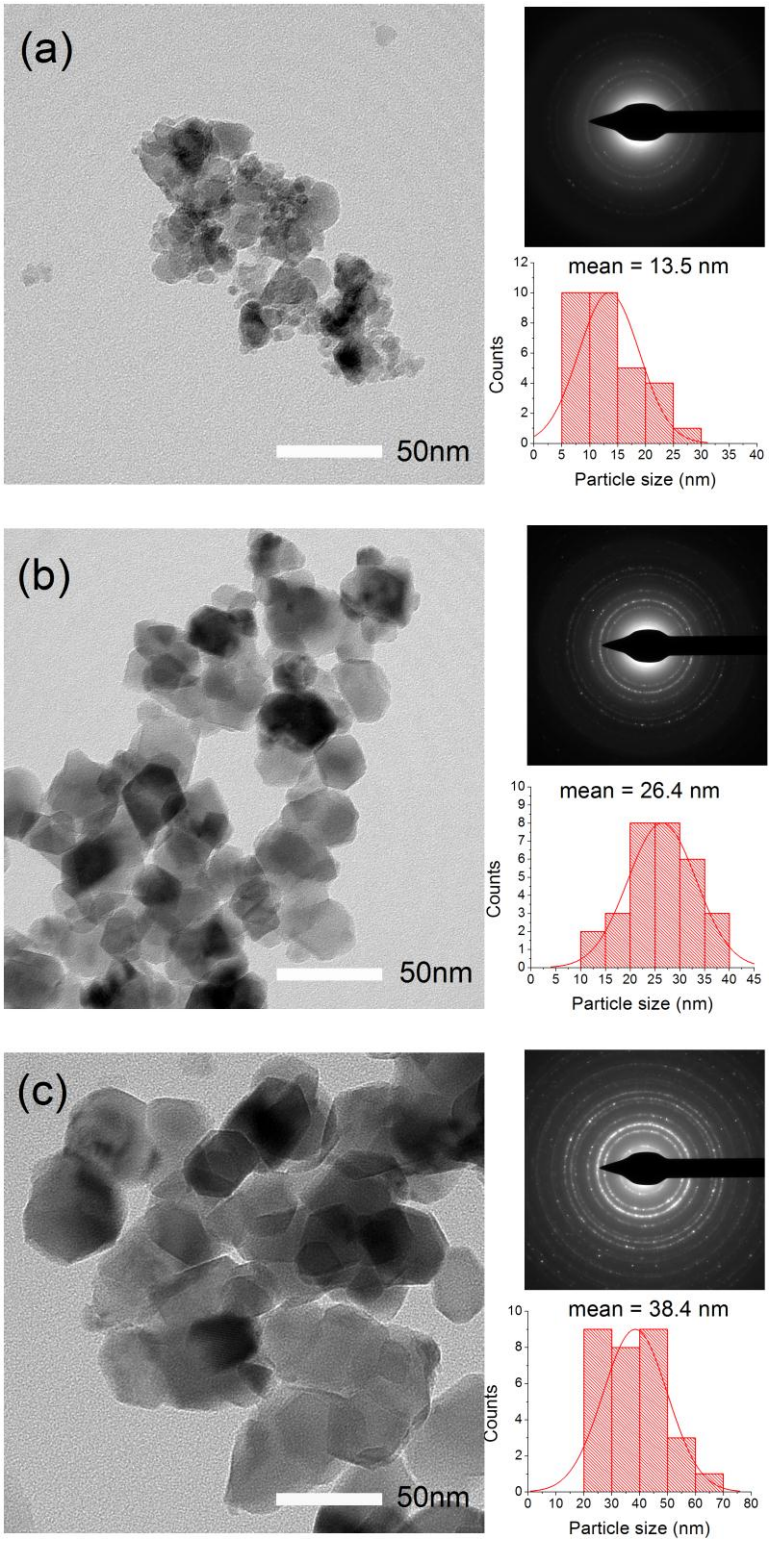

Figure 23 TEM images with selected-area electron diffraction (SAED) patterns and particle size histograms obtained from $CoFe_2O_4$ samples prepared at a pH of 14 and calcined at (a) 300°C (b) 500°C and (c) 700°C.

5.5 The VSM study of magnetic properties of the $CoFe_2O_4$ samples

Figure 24 (a, b) and 25 (b) displays the hysteresis loops obtained from the $CoFe_2O_4$ samples between magnetic fields of -10 kOe and +10 kOe at RT. It is observed that all the $CoFe_2O_4$ samples exhibited FM behavior at RT, with M_S increasing with increasing calcination temperature for all pH concentrations except for the sample synthesized at a pH of 14 which has a decreased M_S at 700°C compared to 500°C, as shown in Figures 24(a). The $CoFe_2O_4$ sample having the largest average crystallite size of ~40 nm exhibited the highest M_S value at 10 kOe of 71.9 emu/g and an H_C value of 1540 Oe for synthesis at a pH of 11 and calcination at 700°C , as shown in Table 3. This highest M_S value obtained from our $CoFe_2O_4$ samples is due mainly to the size effect and is an observation that has been common to other spinel ferrite systems such as $NiFe_2O_4$ [24-26] and $ZnFe_2O_4$ [27]. With increasing particle size, the surface area to volume ratio decreases, resulting in lower magnetization loss due to spin fluctuations in the surface, so the size effect plays an important role in improving the magnetization of this spinel ferrite. As a result, our M_S value of 71.9 emu/g for a crystallite size of ~ 40 nm is higher than the 58.8 emu/g (~69 nm) reported by Rani et al. [28] for material synthesized by the co-precipitation method using CTAB but lower than the 86.9 ± 0.2 emu/g (65.7 ± 1.5 nm) obtained by Akyol et al. [29] for material synthesized by the sol-gel method. It was also lower than the 75.7 emu/g (260 nm) reported by Zhang et al. [30] for material synthesized by the sol-gel auto-combustion method. This suggests that the preparation conditions and the size of the nanoparticles strongly affects the M_S values obtained for $CoFe_2O_4$. In addition, higher M_S values in $CoFe_2O_4$ nanoparticles can also be explained by the magnetic interaction within a mixed distribution of Fe^{3+} and Co^{2+} ions across tetrahedral and octahedral sites.

Table 7 Magnetization and coercivity results obtained from all samples.

Sample		M_S (emu/g) at 10 kOe	H_C (Oe)
pH9	300	32.8	76.8
	500	50.9	454.3
	700	67.5	1527.1
pH11	300	35.8	127.1
	500	58.2	922.1
	700	71.9	1536.1
pH14	300	27.9	468.2
	500	56.1	1091.5
	700	63.9	1221.5

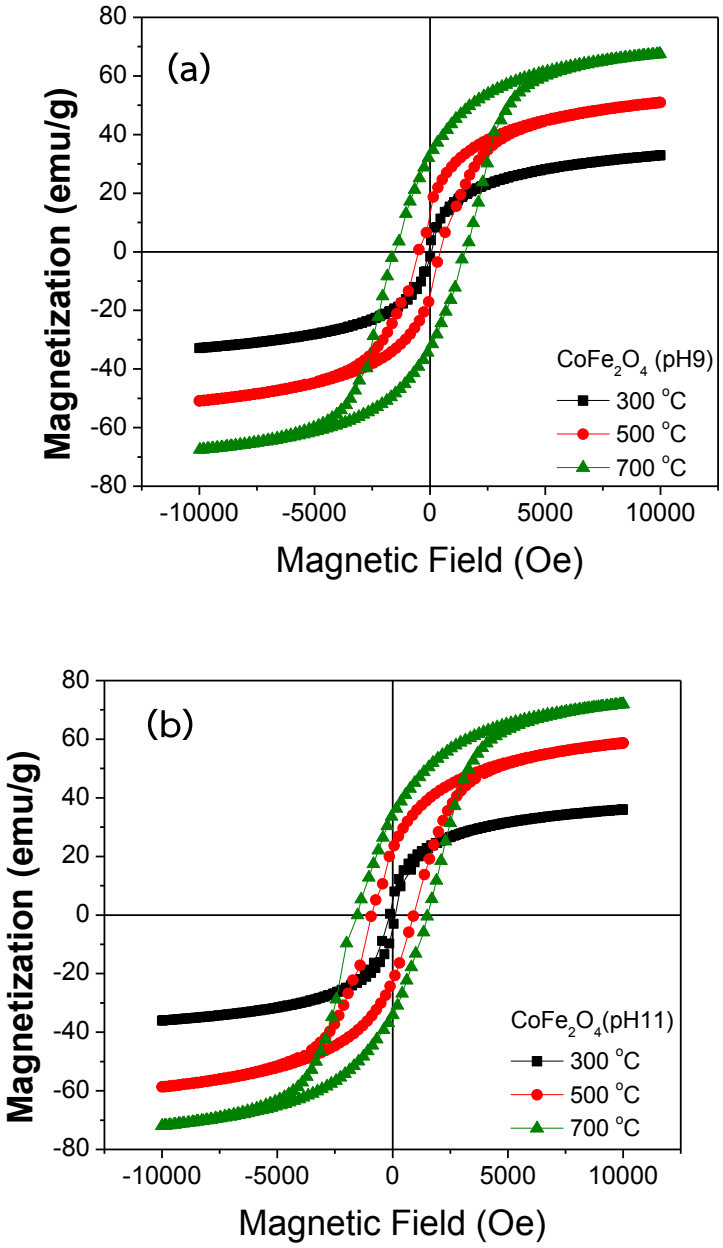

Figure 24 M-H curves measured at room temperature for $CoFe_2O_4$ samples calcined at temperatures between 300°C and 700°C following synthesis at a pH of (a) 9 and (d) 11.

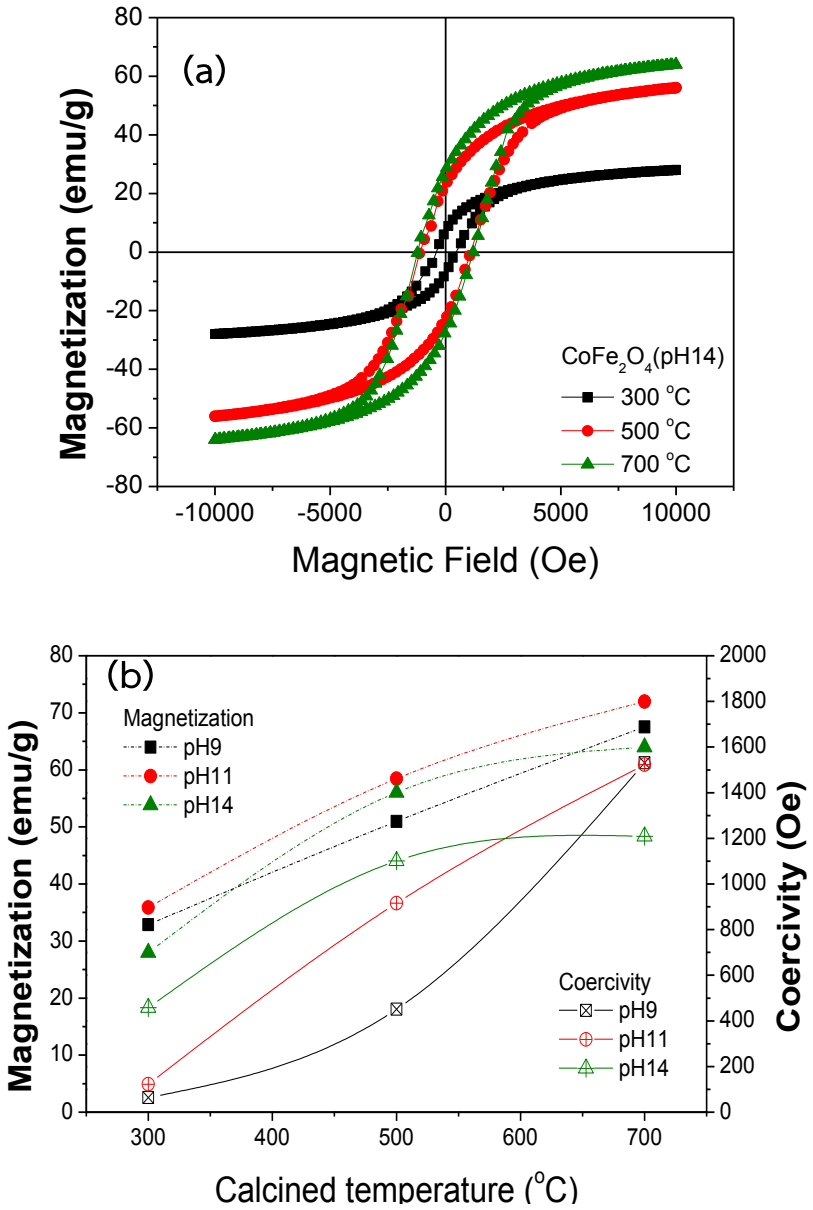

Figure 25 M-H curves measured at room temperature for $CoFe_2O_4$ samples calcined at temperatures between 300°C and 700°C following synthesis at a pH of (a) 14 and (b) shows the magnetization and coercivity results obtained from all samples.

In addition, to study the effect of the calcined temperature on cubic anisotropy constant (K_1) of $CoFe_2O_4$ samples were obtained by fitting the law of Approach to saturation magnetization at the high magnetic field (H) as shown in Figure 26 (a, b) and 27 (a). Which is higher than that of coercive field (H_C), as following equation.

$$M = M_S\left(1-\frac{8K_1^2}{105\mu_0^2 M_S^2 H^2}\right)+kH$$

Where μ_0 is the permeability of free space and the term of kH is known as the forced magnetization. The forced magnetization is caused by a linear increase in the spontaneous magnetization at high magnetic field. The numerical coefficient 8/105 applies to cubic anisotropy of random polycrystalline samples. In general, the forced magnetization term was found to be necessary to fit the hysteresis curves at higher temperatures and higher fields, hence in the present case it has been neglected. It is observed that the K_1 values of $CoFe_2O_4$ samples increased with increasing calcination temperature for each pH concentration, as shown in Figure 27(b). The higher K_1 values for $CoFe_2O_4$ nanoparticles is expected because the strong anisotropy of cobalt ferrite is primarily due to the presence of Co^{2+} ions on the octahedral sites of the spinel structure since they have high spin ligand fields and possess seven d electrons with three of them unpaired. The Fe^{3+} ions contribute as well, however here the coupling depends on the site since the A site has tetrahedral symmetry and the B site has octahedral symmetry. Thus, the contribution to the magnetic anisotropy from L–S couplings in Fe^{3+} ions may vary with cation distribution.

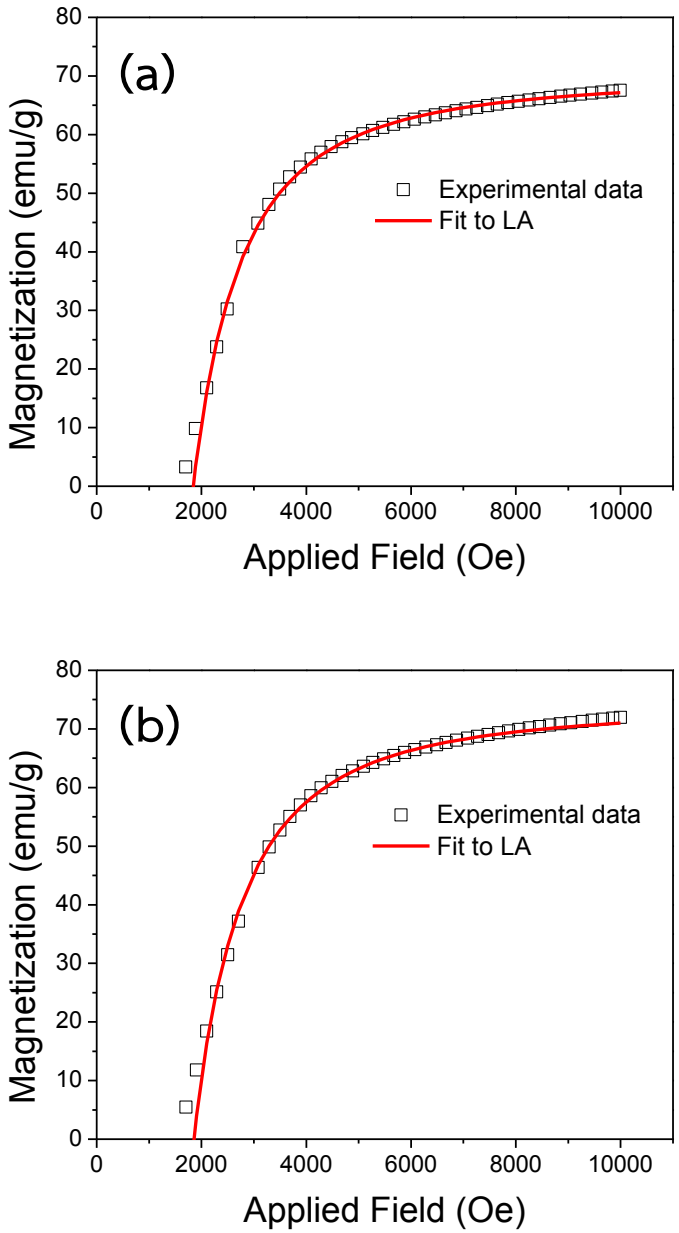

Figure 26 Fitting the law of Approach to saturation magnetization of $CoFe_2O_4$ samples calcined at 700°C following synthesis at a pH of (a) 9 and (b) 11

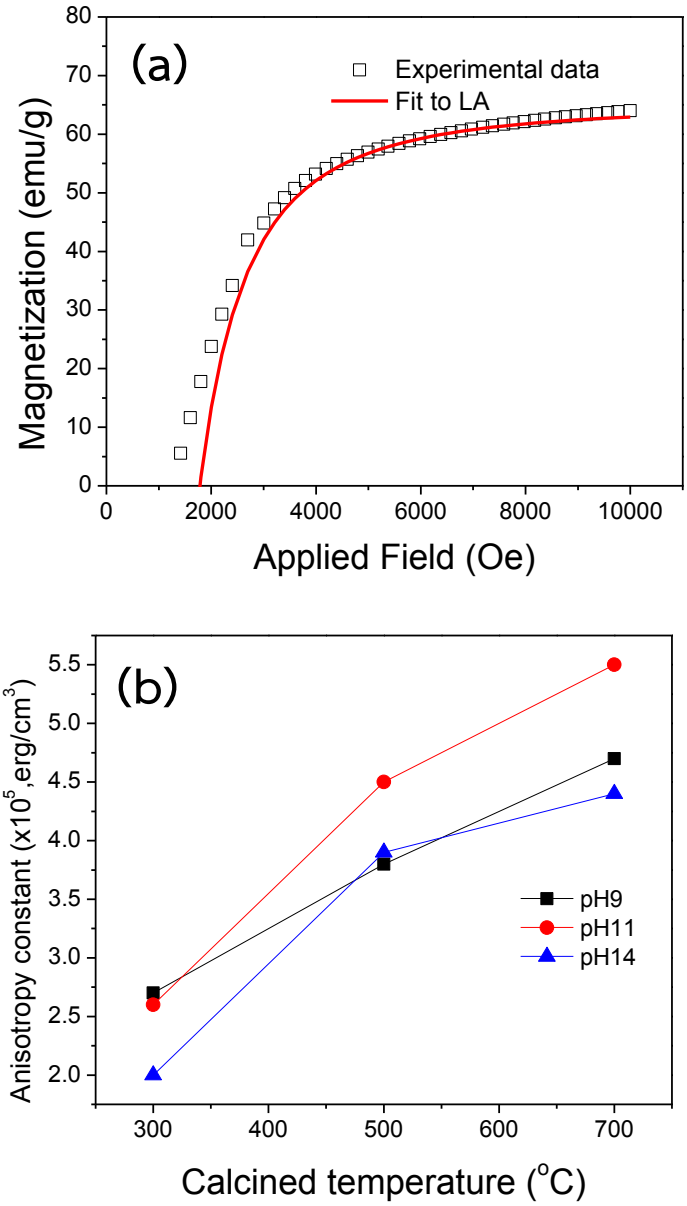

Figure 27 (a) Fitting the law of Approach to saturation magnetization of $CoFe_2O_4$ samples calcined at 700°C following synthesis at a pH of 9 and (b) Variation of anisotropy constant of all samples as a function of the calcined temperature.

5.6 The XRD study of fly ash and $CoFe_2O_4$-geopolymer composites

The XRD investigation of geopolymer composites aged 28 days was shown in Figure 28-30. The patterns of geopolymer showed amorphous phase without crystalline peaks, whereas that of fly ash contained amorphous phase with certain crystalline phases of quartz (SiO_2), magnesioferrite ($MgFe_2O_4$), anhydrite ($CaSO_4$), hatrurite ($Ca_3(SiO_4)O$), porlandite ($Ca(HO)_2$), and calcium oxide (CaO). The XRD patterns of all geopolymer composites showed low intensity crystalline peaks and most of them were amorphous phases as illustrated by the broad humps from 22° to 38° (2θ) indicating the formation of alumino-silicate frame work. The crystalline peak of calcium-silicate-hydrate (C-S-H) at 2θ 29.6° was found as similar to the main hydration product in cement system. Therefore, the XRD results suggested that the geopolymerization and the hydrate reaction occurred concurrently.

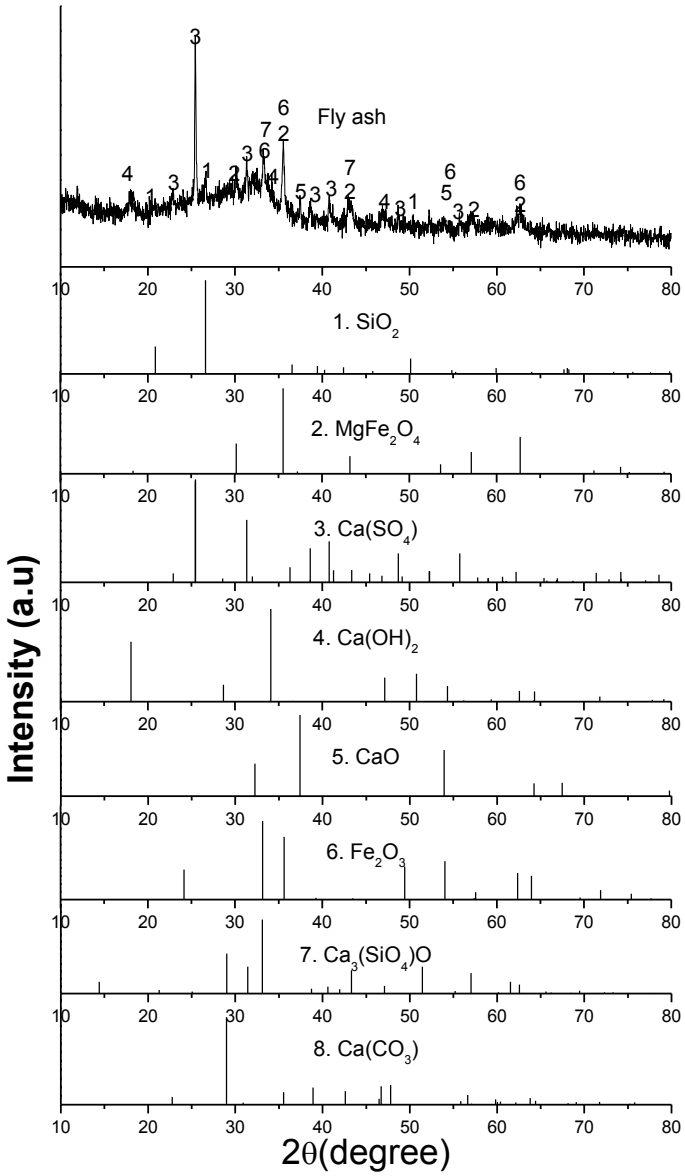

Figure 28 XRD profiles of fly ash powders.

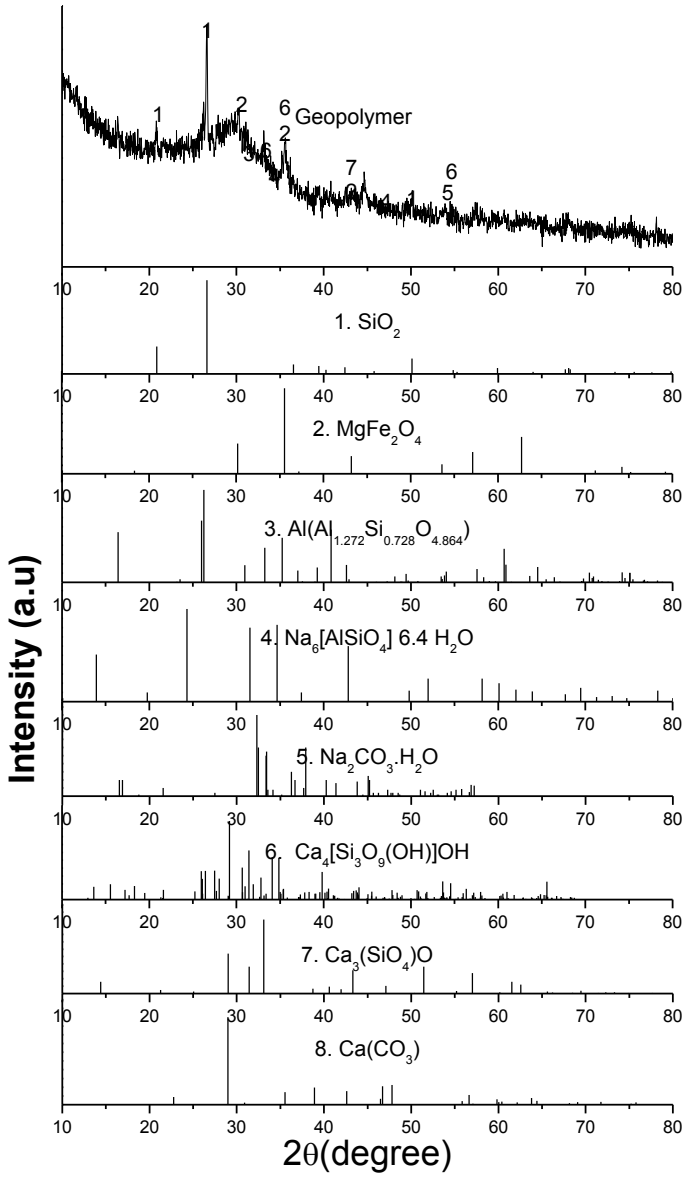

Figure 29 XRD profiles of of $CoFe_2O_4$-geopolymer composites.

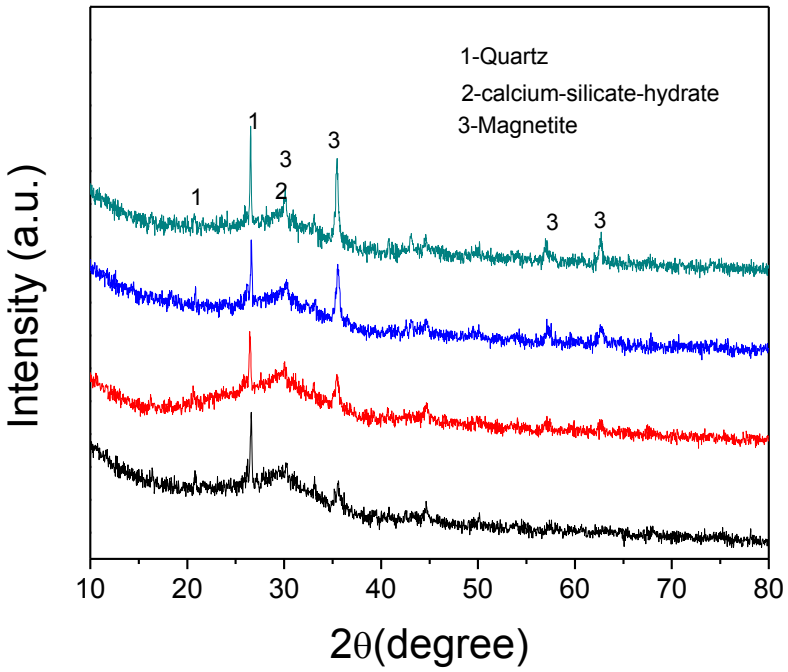

Figure 30 XRD profiles of of $CoFe_2O_4$-geopolymer composites.

5.7 The FT-IR study of $CoFe_2O_4$-geopolymer composites

Figure 31 presents the FTIR spectra of fly ash and $CoFe_2O_4$-geopolymer composites containing with 0%, 1%, 3% and 5%wt of $CoFe_2O_4$ nanopowders. For Fly ash, the absorbance band at 927 cm^{-1} is assigned to the asymmetric stretching of (Si,Al)-O-Si in glass, which may partially overlap with the bands of mullite and quartz at this position. The bands appear at around 1391 cm^{-1} are assigned to the vibrations of CO_3^{2-} groups. The broad band centred at 3327 cm^{-1} is attributed to the overlap of the symmetric stretching and the asymmetric stretching of O-H bonds of absorbed water.

After activation, the broad absorbance band of the $CoFe_2O_4$-geopolymer composites sample shifts towards a lower frequency region, centred at 984 cm^{-1}. This shift from a higher frequency region to a lower frequency region is a common signal for the occurrence of geopolymerisation. The exact shifting position and span depends on the source fly ash (more specifically the Si/Al ratio in the glassy phases of fly ash) and the reaction conditions. The final position of this main band can slightly increase with curing time extending. The new bands appear at around 1671 cm^{-1} are assigned to the vibrations of and -OH groups. The -OH groups present as structural water in sodium alumino silicate gels (N-A-S-H).

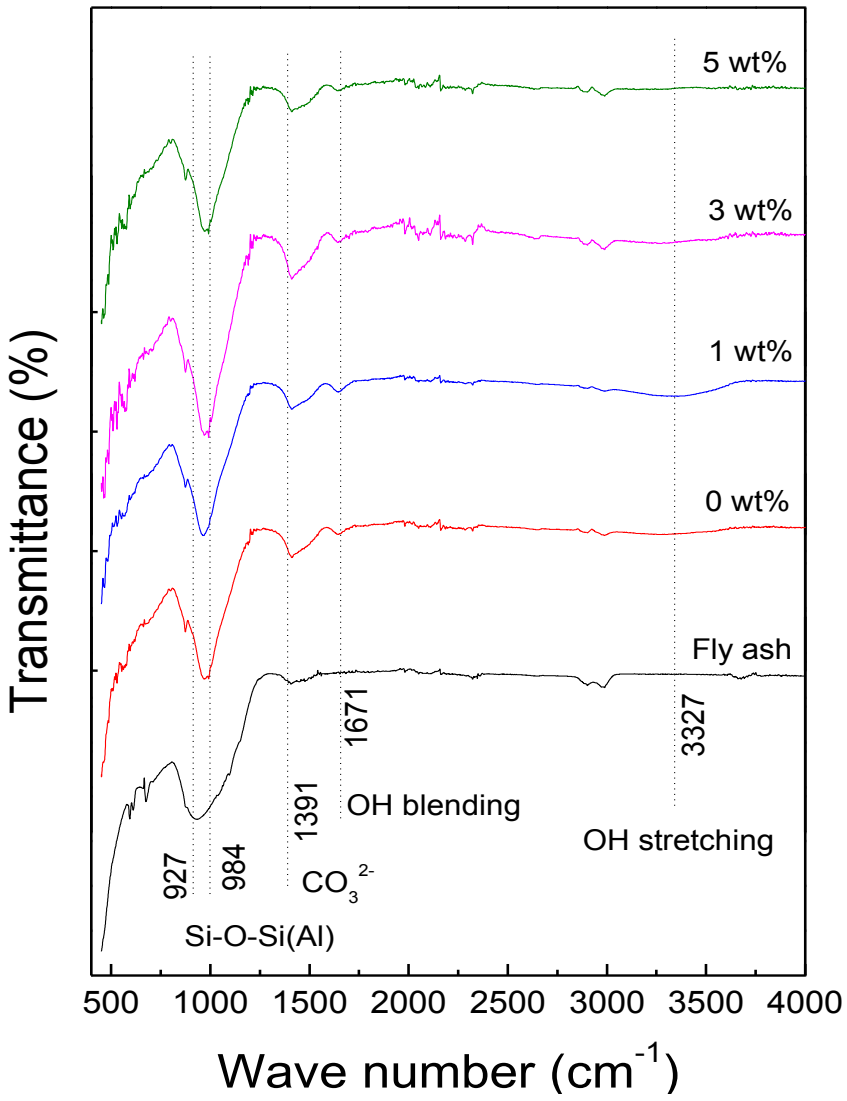

Figure 31 FT-IR spectra of Fly ash and $CoFe_2O_4$-geopolymer composites.

5.8 Photography images and SEM of $CoFe_2O_4$-geopolymer composites

The photography of geopolymer composites with various $CoFe_2O_4$ additions aged 28 days were shown in Figure 32. It can be seen that the color of geopolymer have a gray color. When the $CoFe_2O_4$ nanopowders were added, the color of geopolymer changed from gray to black color with increases $CoFe_2O_4$ nanopowders. It indicated that the $CoFe_2O_4$ nanopowders well dispersed in geopolymer matrix. The SEM images of geopolymer composites aged 28 days with varied $CoFe_2O_4$ additions were shown in Fig. 33 and 34. The microstructure of all samples showed heterogeneous containing with the alumino- silicate matrix, un-reacted fly ash and small pore of fly ash particles. All composite samples are not observed the agglomeration of $CoFe_2O_4$ nanopowders, indicating that well dispersed in geopolymer matrix. In addition, the cracks observed in the microstructure were believed to be caused by the compressive strength measurement prior to the morphology investigation.

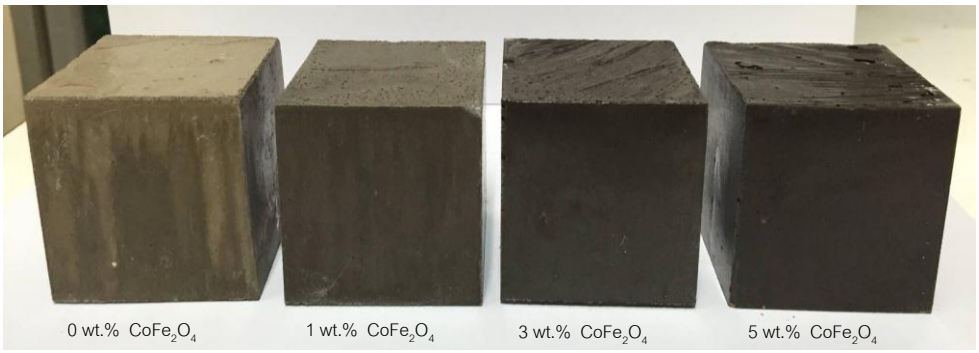

Figure 32 Photography of geopolymer composites with various $CoFe_2O_4$ content.

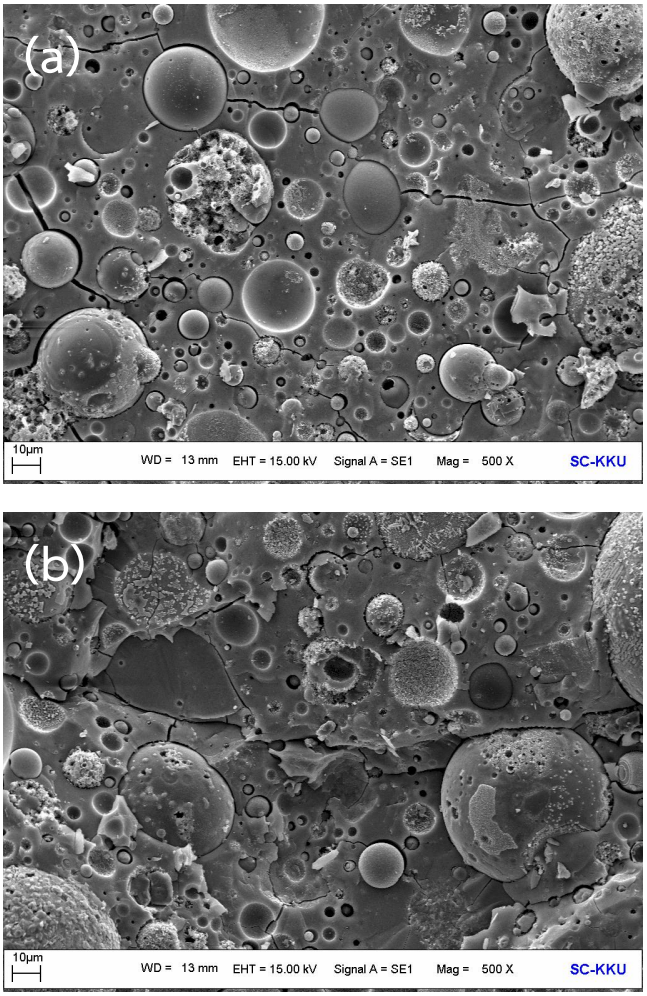

Figure 33 SEM images of fly ash based geopolymer composites containing with $CoFe_2O_4$ nanopowders of (a) 0 %wt and (b) 1 %wt.

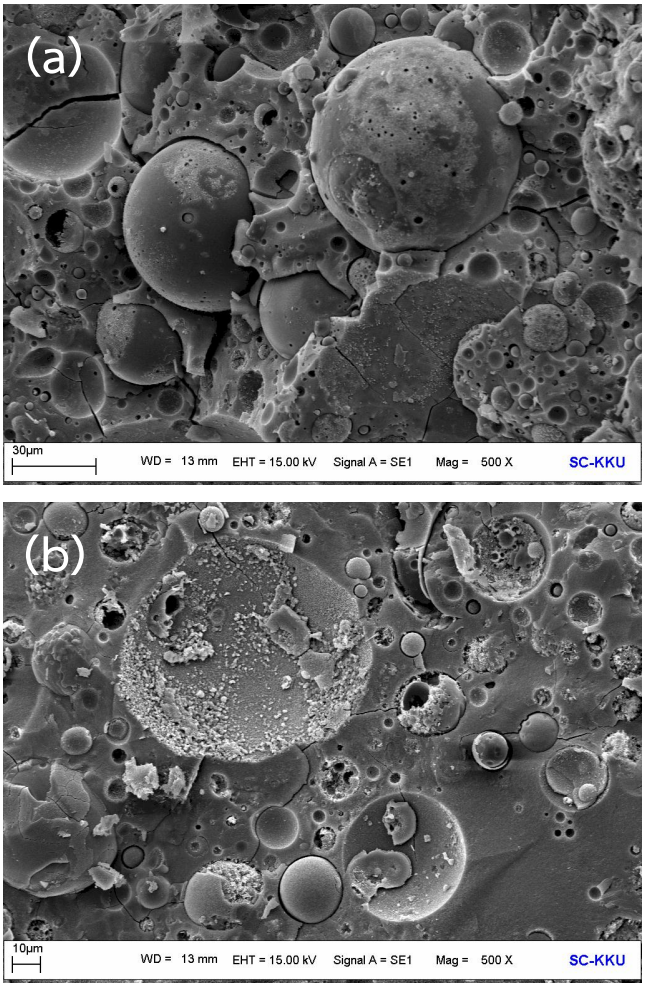

Figure 34 SEM images of fly ash based geopolymer composites containing with $CoFe_2O_4$ of (a) 3 %wt and (b) 5 %wt.

5.9 The VSM study of $CoFe_2O_4$-geopolymer composites

Figure 35 (a) displays the hysteresis loops obtained from the $CoFe_2O_4$ samples between magnetic fields of -10 kOe and +10 kOe at room temperature. The ferromagnetic behavior of geopolymer without $CoFe_2O_4$ nanopowders were observed because the compound minerals of fly ash consist of Fe_2O_3 and $MgFe_2O_4$. M_S and H_C value of geopolymer without $CoFe_2O_4$ nanopowders are 1.41 emu/g and 106 Oe, respectively. For geopolymer with $CoFe_2O_4$ nanopowders of 1, 3 and 5 %wt also exhibited Ferromagnetic behavior with M_S and H_c increasing with increasing $CoFe_2O_4$ content (Figure 35 (b)). The M_S values of all composites are 2.14, 2.94 and 3.94 emu/g for 1, 3 and 5 %wt, respectively. For the H_c value of all composites are 199, 405 and 629 Oe for 1, 3 and 5 %wt, respectively. The increase of magnetic value is not related with the compressive strength of composites samples.

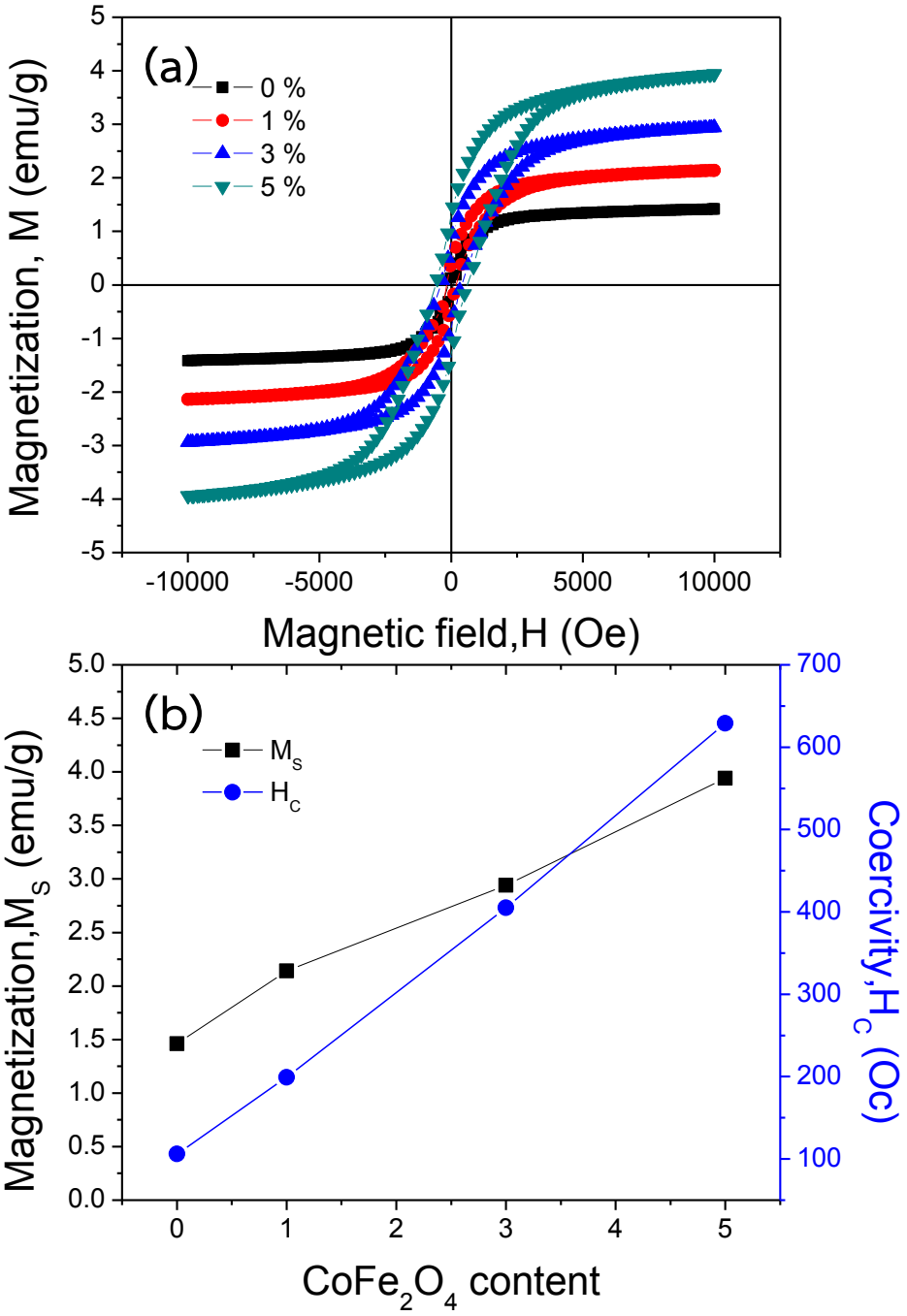

Figure 35 (a) M-H curves measured at room temperature for $CoFe_2O_4$-geopolymer composites and (b) Variation of M_S and H_c of all samples as a function of the $CoFe_2O_4$ content.

5.10 Dielectric properties of $CoFe_2O_4$ –geopolymer composites

Figure 36 (a) and (b) shows the values of dielectric constant and dissipation factor as functions of frequency for the $CoFe_2O_4$ –geopolymer composites. These values were measured at 28 days after mixing. The values of dielectric constant rapidly decreased with the increased frequency. Then, the rate of decrease slowed down at higher frequencies and decreased till reaching near-constant values. Generally, there are four mechanisms of polarisation; ionic, dipolar or molecular, electronic and atomic, and interfacial and double layer polarisations. Different frequency ranges generate different polarisation mechanisms. At low frequencies, the molecules get enough time to rotate and orient themselves in the direction of the applied alternating electric current. The dipoles can be fully polarised and the dielectric constant is maximum. As the frequency increases, the electric current quickly alternates its direction and there is not enough time available for the molecules to follow and align in the direction of the exerted field; thus, the polarisability will be reduced. At low frequencies, the decrease in the dielectric values with change in frequency can be attributed to the interfacial and the double layer polarisation mechanisms. The $CoFe_2O_4$–geopolymer composites are composed of several phases as demonstrated in Figure 29 and 30. These phases include; alumino silicate matrixes, un-reacted fly ash particles, and pores. When an electric field is applied to the sample, and because of the difference in the electrical conductivity between the matrix phases, charges move and build up at the interface of the different phases.

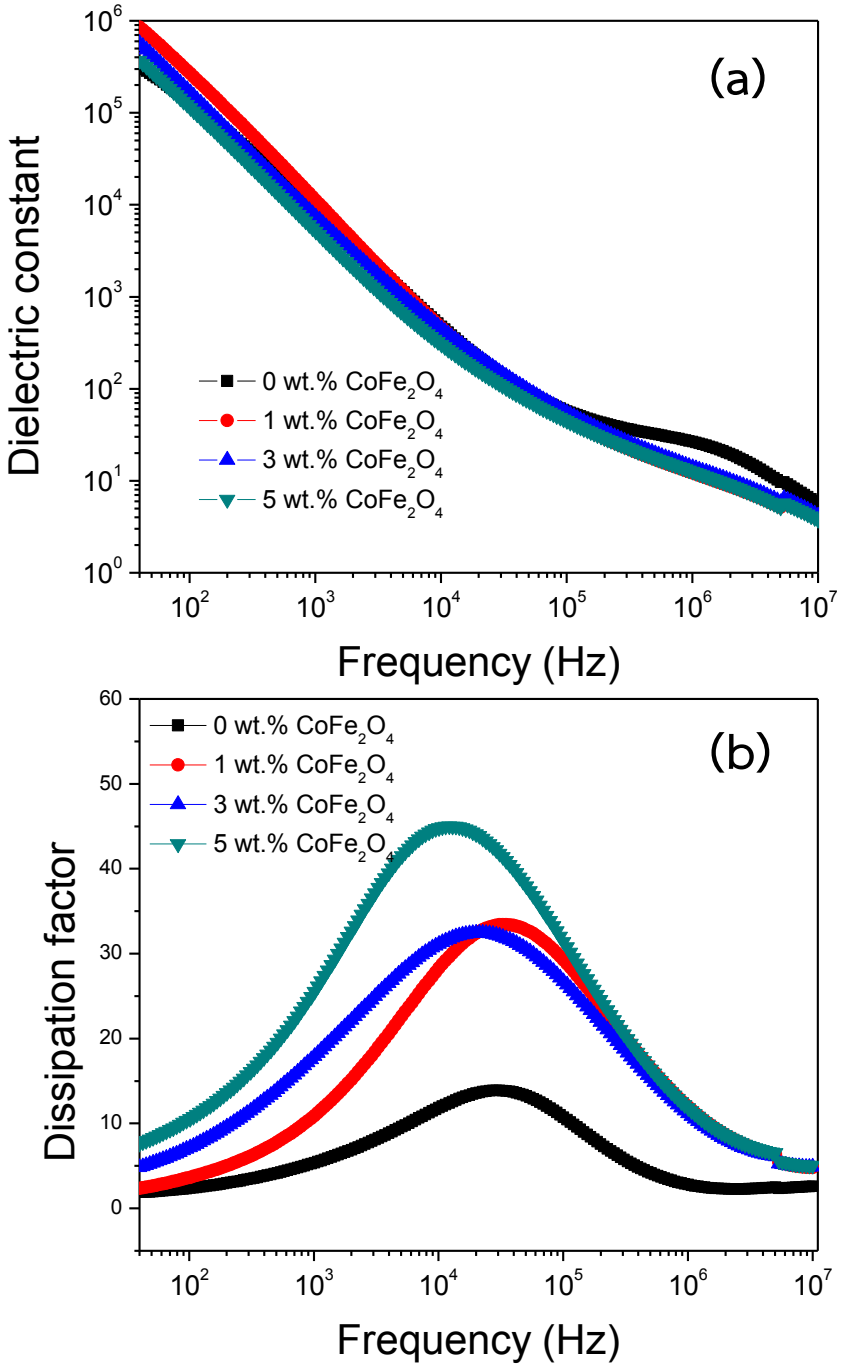

Figure 36 The values of (a) dielectric constant and (b) dissipation factor as functions of frequency for the $CoFe_2O_4$–geopolymer composites.

5.11 Nyquist plots of $CoFe_2O_4$–geopolymer composites

Figure 37 and 38 shows the Nyquist plots of this geopolymer at the age of 28 day. Three parts were observed which can be identified as bulk resistance, fly ash resistance and electrode resistance. The bulk resistance was observed from intercept on real axis at high frequency and found to be 250, 150, 165 and 180 for 0, 1, 3 and 5% of $CoFe_2O_4$ nanopowders, respectively. The intercept of the geopolymer without $CoFe_2O_4$ nanopowders is higher than that of all samples. A larger diameter of the high-frequency arc implies a higher bulk resistance. Figure 37 and 38 shows that the bulk electrical resistance of this geopolymer increases with increasing $CoFe_2O_4$ content. Ii has been reported that the diameters of the high-frequency arcs are affected by the content of CaO in the fly ash. The higher the content of CaO in the fly ash, the smaller the diameter of the high-frequency arc of the Nyquist plot of the electrical impedance. Therefore, the geopolymer with high CaO content has a higher resistance at the early age. However, at the late age, the fast reaction rate of the CaO diminishes. Because that Ca^{2+} ions were not integrate into the geopolymer chains, Geopolymer made of fly ash with higher calcium content may contain more free Ca^{2+} ions and therefore have higher conductivity, as indicated by the smaller diameter of the high-frequency arc. As a result, more free Na^{+} ions and other ions released from the fly ash can be consumed, and more reaction products can be generated to reduce the porosity of the geopolyers. For this work, the higher the content of CaO in the fly ash, the higher the diameter of the high-frequency arc of the Nyquist plot of the electrical impedance.

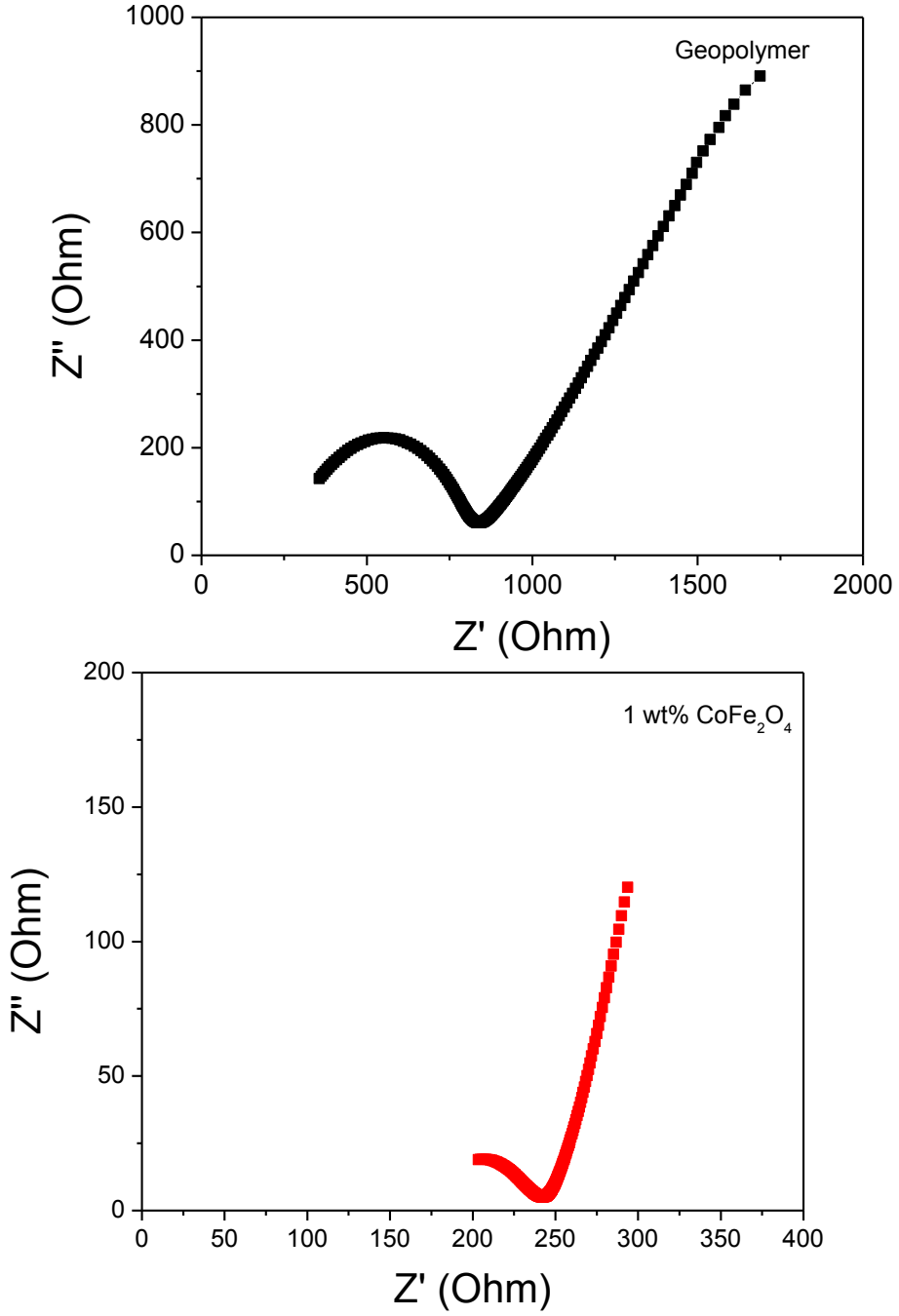

Figure 37 The Nyquist plots of the geopolymer composites containing with $CoFe_2O_4$ nanopowders (a) 0 % and (b) 1 %wt.

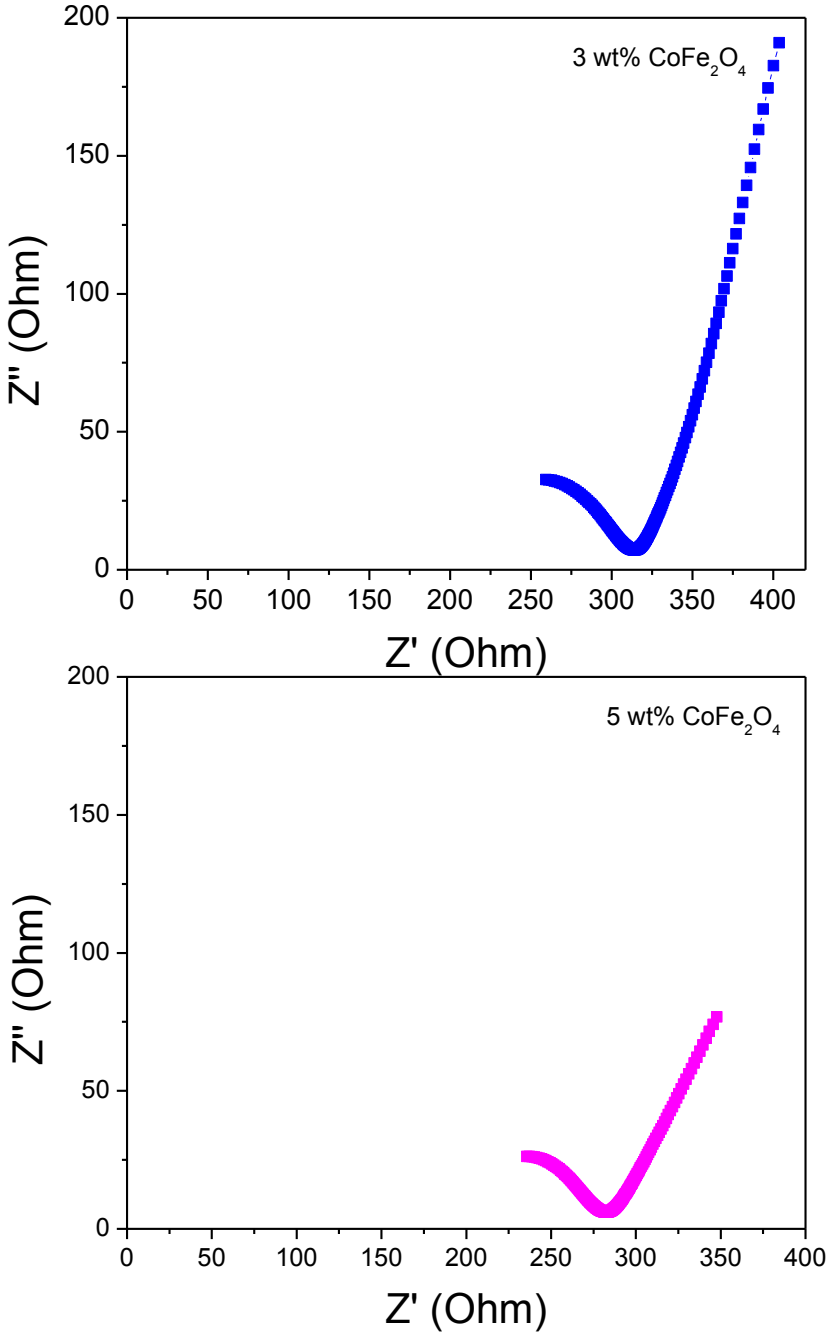

Figure 38 The Nyquist plots of the geopolymer composites containing with $CoFe_2O_4$ nanopowders (a) 0 %wt and (b) 1 %wt.

5.12 The compressive strength of $CoFe_2O_4$-geopolymer

Figure 39 showed compressive strength, plotting as a function of $CoFe_2O_4$ nanoparticles containing with 0, 1, 3 and 5 %wt. The compressive strength values of geopolymer composites are 47.3, 42.5, 42.7 and 49.5 for 0, 1, 3 and 5 %wt. $CoFe_2O_4$ nanoparticles, respectively. It can be seen that compressive strength deceased with the replacing $CoFe_2O_4$ nanoparticles at 1 %wt. And then the increasing quantity of $CoFe_2O_4$ nanoparticles up to 5%, the compressive strength is higher than that of geopolymer without $CoFe_2O_4$ nanoparticles for 5 %wt. $CoFe_2O_4$ nanoparticles. From the XRD result indicated that $CoFe_2O_4$ nanoparticles not affected on phase of geopolymer. Therefore, this issue is because nanoparticles due to their high surface energy have the tendency towards agglomeration. When nanoparticles are over added to the paste it is not uniformly distributed in geopolymer paste and due to agglomeration, weak zone appear in the samples. However, with the increase of $CoFe_2O_4$ nanoparticles which the strength of geopolymer increased can be described as follows that the addition of $CoFe_2O_4$ nanoparticles fills the voids of N-A-S-H gel structure are denser and compact.

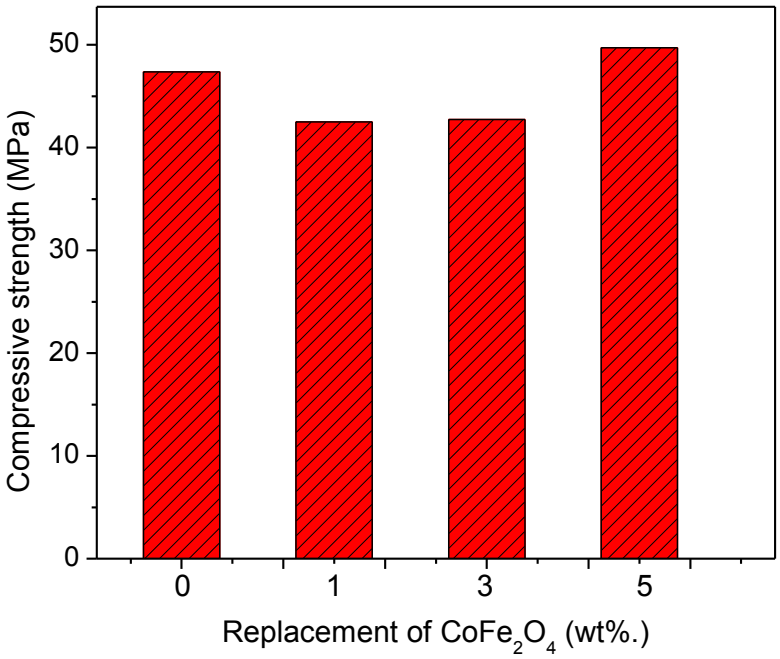

Figure 39 Compressive strength of the geopolymer composites containing with $CoFe_2O_4$ nanopowders 0, 1, 3 and 5 %wt.

6. References

[1] J. Deja, A. Uliasz-Bochenczyk, E. Mokrzycki, CO_2 emissions from Polish cement industry, International Journal of Greenhouse Gas Control, 4 (2010) 583–588.

[2] E. Benhelal, G. Zahedi, E. Shamsaei, A. Bahadori, Global strategies and potentials to curb CO_2 emissions in cement industry, Journal of Cleaner Production, 51 (2013) 142–161.

[3] J. Davidovits, Geopolymers and geopolymeric materials, Journal of Thermal Analysis, 35 (1989) 429–441.

[4] K. Srinivasan, A. Sivakumar, Geopolymer Binders: A Need for Future Concrete Construction, ISRN Polymer Science, 2013 (2013) 509183.

[5] P. Chindaprasirt, T. Chareerat, V. Sirivivananon, Workability and strength of coarse high calcium fly ash geopolymer, Cement and Concrete Composites, 29 (2007) 224–229.

[6] A. Sathonsaowaphak, P. Chindaprasirt, K. Pimraksa, Workability and strength of lignite bottom ash geopolymer mortar, Journal of Hazardous Materials, 168 (2009) 44–50.

[7] U. Rattanasak, P. Chindaprasirt, Influence of NaOH solution on the synthesis of fly ash geopolymer, Minerals Engineering, 22 (2009) 1073–1078.

[8] S. Detphan, P. Chindaprasirt, Preparation of fly ash and rice husk ash geopolymer, International Journal of Minerals, Metallurgy and Materials formerly Journal of University of Science and Technology Beijing, Mineral Metallurgy Material, 16 (2009) 720–726.

[9] S. Songpiriyakit, T. Kubprasit, C. Jaturapitakkul, P. Chindaprasirt, Compressive strength and degree of reaction of biomass and fly ash based geopolymer, Construction and Building Materials, 24 (2010) 236–240.

[10] U. Rattanasak, K Pankhet, P. Chindaprasirt, Effect of chemical admixtures on properties of high-calcium fly ash geopolymer, International Journal of Minerals, Metallurgy and Materials, 18 (2011) 364–369.

[11] P. Chindaprasirt, P. De Silva, K. Sagoe-Crentsil, S. Hanjitsuwan, Effect of SiO_2 and Al_2O_3 on the setting and hardening of high calcium fly ash based geopolymer systems, Journal of Materials Science, 47 (2012) 4876–4883.

[12] T. Phoo-ngernkham, P. Chindaprasirt, V. Sata, S. Hanjitsuwan, S. Hatanaka, The effect of adding nano-SiO_2 and nano-Al_2O_3 on properties of high calcium fly ash geopolymer cured at ambient temperature, Materials and Design, 53 (2014) 58–65.

[13] Y. Huang, M. Han, The influence of alpha-Al_2O_3 addition on microstructure, mechanical and formaldehyde adsorption properties of fly ash-based geopolymer products, Journal of Hazardous Materials, 193 (2011) 90–94.

[14] S. Pangdaeng, T. Phoo-ngernkham, V. Sata, P. Chindaprasirt, Influence of curing conditions on properties of high calcium fly ash geopolymer containing Portland cement as additive, Materials and Design, 53 (2014) 269–274.

[15] A. Folli, C. Pade, T. B. Hansen, T. De Marco, D .E. Macphee, TiO_2 photocatalysis in cementitious systems: Insights into self-cleaning and depollution chemistry. Cement and Concrete Research, 42 (2012) 539–548.

[16] M. Smits, C. K. Chan, T. Tytgat, B. Craeye, N. Costarramone, S. Lacombe, S. Lenaerts, Photocatalytic degradation of soot deposition: Self-cleaning effect on titanium dioxide coated cementitious materials, Chemical Engineering Journal, 222 (2013) 411–418.

[17] M. Z. Guo, C. S. Poon, Photocatalytic NO removal of concrete surface layers intermixed with TiO_2, Building and Environment, 70 (2013) 102–109.

[18] Z. Li, D. Zhang, K. Wu, Cement-Based 0–3 Piezoelectric Composites. Journal of the American Ceramics Society, 85 (2002) 305–313.

[19] A. Chaipanich, N. Jaitanong, T. Tunkasiri, Fabrication and properties of PZT-Ordinary Portland Cement composites, Materials Letters, 61 (2007) 5206–5208.

[20] R. Rianyoi, R. Potong, N. Jaitanong, R. Yimnirun, Dielectric, ferroelectric and piezoelectric properties of 0–3 barium titanate-Portland cement composites, Applied Physics A, 104 (2011) 661–666.

[21] S. Hunpratub, T. Yamwong, S. Srilomsak, S. Maensiri, P. Chindaprasirt, Effect of particle size on the dielectric and piezoelectric properties of 0-3BCTZO/cement composites, Ceramics International, 40 (2014)1209–1213.

[22] B. Han, K. Zhang, X. Lu, Enhance the Thermal Storage of Cement-Based Composites with Phase Change Materials and Carbon Nanotubes, Journal of Solar Energy Engineering, 135 (2013) 024505.

[23] B. Han, X. Yu, E. Kwon, A self-sensing carbon nanotube/cement composite for traffic monitoring, Nanotechnology, 20 (2009) 445501.

[24] B. Han, K. Zhang, X. Yu, E. Kwon, J. Ou, Electrical characteristics and pressure-sensitive response measurements of carboxyl MWNT/cement composites, Cement and Concrete Composites, 34 (2012) 794–800.

[33] T. W. Tombler, C. Zhou, L. Alexseyev, J. Kong, H. Dai, L. Liu, C. S. Jayanthi, M. Tang , S. Y. Wu, Reversible electromechanical characteristics of carbon nanotubes under local-probe manipulation, Nature, 405 (2000) 769–772.

[34] J. Cao, Q. Wang, H. Dai, Electromechanical properties of metallic, quasimetallic, and semiconducting carbon nanotubes under stretching, Physics Review Letters, 90 (2003) 157601.

[35] S. Wen, D. D. L. Chung, Piezoresistivity in continuous carbon fiber cement-matrix composite Cement Concrete Research, 29 (1999) 445–9.

[36] D. D. L. Chung, Electromagnetic interference shielding effectiveness of carbon materials, Carbon, 39 (2001) 279–285.

[37] J. Y. Cao, D. D. L. Chung, Coke powder as an admixture in cement for electromagnetic interference shielding, Carbon, 41 (2003) 2433–6.

[38] Q. Li, J. Pang, B. Wang, D. Tao, X. Xu, L. Sun, J. Zhai, Preparation, characterization and microwave absorption properties of barium-ferrite-coated fly-ash cenospheres, Advanced Powder Technology, 24 (2013) 288–294.

[39] S. J. Son, J. Reichel, B. He, M. Schuchman, S.B. Lee, Magnetic Nanotubes for Magnetic-Field-Assisted Bioseparation, Biointeraction, and Drug Delivery Journal of the American Chemical Society,127 (2005) 7316.

[40] D. Li, T. Herricks, Y.N. Xia, Magnetic nanofibers of nickel ferrite prepared by electrospinning Applied Physics Letters ,83 (2003) 4586.

[41] J. R. Liu, M. Itoh, M. Terada, T. Horikawa, K.I. Machida, Enhanced electromagnetic wave absorption properties of Fe nanowires in gigaherz range, Applied Physics Letters, 91(2007) 093101.

[42] Z. L. Wang, X. J. Liu, M. F. L, P. Chai, Y. Liu, X. F. Zhou, Preparation of One-Dimensional $CoFe_2O_4$ Nanostructures and Their Magnetic Properties Journal of Physical Chemistry C, 112 (2008) 15171.

[43] V. Blanco-Gutiérrez, J. A. Gallastegui, P. Bonville, M. J. Torralvo-Fernández, R. Sáez-Puche, MFe2O4 (M: Co^{2+}, Ni^{2+}) Nanoparticles: Mössbauer and X-ray Absorption Spectroscopies Studies and High-Temperature Superparamagnetic Behavior, Journal of Physical Chemistry C, 2012, 116, 24331-24339.

[44] M. Houshiar, F. Zebhi, Z. J. Razi, A. Alidoust, Z. Askari, Synthesis of cobalt ferrite ($CoFe_2O_4$) nanoparticles using combustion, coprecipitation, and precipitation methods: A comparison study of size, structural, and magnetic properties, Journal of magnetism and magnetic materials, 371 (2014) 43-48.

[45] M. Vadivel, R. Ramesh Babu, K. Sethuraman, K. Ramamurthi, M. Arivanandhan, Synthesis, structural, dielectric, magnetic and optical properties of Cr substituted $CoFe_2O_4$ nanoparticles by co-precipitation method Journal of Magnetism and Magnetic Materials, 362 (2014) 122-129.

[46] C. Pereira, A. M. Pereira, C. Fernandes, M. Rocha, R. Mendes, M. P. Fernández-García, A. Guedes, P. B. Tavares, J. M. Grenèche, J. P. Araújo, and C. Freire, Superparamagnetic MFe_2O_4 (M = Fe, Co, Mn) Nanoparticles: Tuning the Particle Size and Magnetic Properties through a Novel One-Step Coprecipitation Route, Chemistry of Materials 24, (2012) 1496-1504.

[47] S. H. Xiao, W. F. Jiang, L. Y. Li, X. J. Li, Low-temperature auto-combustion synthesis and magnetic properties of cobalt ferrite nanopowder, Materials Chemistry and Physics, 106 (2007) 82–87

[48] S. Phumying, S. Labuayai, E. Swatsitang, V. Amornkitbamrung, S. Maensiri , Nanocrystalline spinel ferrite (MFe_2O_4, M = Ni, Co, Mn, Mg, Zn) powders prepared by a simple aloe vera plant-extracted solution hydrothermal route Materials Research Bulletin, 48 (2013) 2060-2065.

[49] Y. Tang, X. Wang, Q. Zhang, Y. Lia, H. Wang, Solvothermal synthesis of $Co_{1-x}Ni_xFe_2O_4$ nanoparticles and its application in ammonia vapors detection, Progress in Natural Science: Materials International, 22(1) (2012) 53–58.

[50] S. Yáñez-Vilar, M. Sánchez-Andújar, C. Gómez-Aguirre, J. Mira, M.A. Señarís-Rodríguez, S. Castro-García, A simple solvothermal synthesis of MFe_2O_4 (M=Mn, Co and Ni) nanoparticles Journal of Solid State Chemistry, 182, (2009) 2685-2690

[51] M. Sangmanee, S. Maensiri, Nanostructures and magnetic properties of cobalt ferrite ($CoFe_2O_4$) fabricated by electrospinning, Applied Physics A, 97 (2009) 167–77.

[52] J. Xiang, Y. Chu, X. Shen , G. Zhou, Y.Guo, Electrospinning preparation, characterization and magnetic properties of cobalt–nickel ferrite ($Co_{1-x}Ni_xFe_2O_4$) nanofibers, Journal of Colloid and Interface Science, 376 (2012) 57–61.

[53] Y. W. Ju, J. H. Park, H. R. Jung, S. J. Cho, W. J. Lee, Fabrication and characterization of cobalt ferrite ($CoFe_2O_4$) nanofibers by electrospinning, Materials Science and Engineering: B, 147 (2008) 7–12.

[54] P. Laokul, V. Amornkitbamrung, S. Seraphin, S. Maensiri, Characterization and magnetic properties of nanocrystalline $CuFe_2O_4$, $NiFe_2O_4$, $ZnFe_2O_4$ powders prepared by the Aloe vera extract solution Current Applied Physics, 11 (2011) 101–108.

[55] T. Prabhakaran, J. Hemalatha, Chemical control on the size and properties of nano $NiFe_2O_4$ synthesized by sol–gel autocombustion method, Ceramics International, 40 (2014) 3315-3324.

Output จากโครงการวิจัยที่ได้รับทุนจาก สกว.

---

1. ผลงานตีพิมพ์ในวารสารวิชาการนานาชาติ

- **Sitchai Hunpratub**, Sumalin Phokha, Pinit Kidkhunthod and Prinya Chindaprasirt, The effect of synthesis pH on the magnetic properties of $CoFe_2O_4$ nanoparticles, Ceramics International, Manuscript. อยู่ในฐานข้อมูล ISI/Scopus, IF2016/Q1 = 2.758

2. การนำผลงานวิจัยไปใช้ประโยชน์ (ดังเอกสารที่แนบ)

- เชิงวิชาการ (มีการพัฒนาการเรียนการสอน/สร้างนักวิจัยใหม่)